Separation of the Icelandic Coastal Current from the Reykjanes Peninsula

Authors: Michael M. Whitney[a*]

Affiliations: [a]Department of Marine Sciences, University of Connecticut, Groton, CT, USA

Correspondence: *Michael M. Whitney
1080 Shennecossett Rd.
Groton, CT, USA
michael.whitney@uconn.edu

Abstract

The Icelandic Coastal Current (ICC) is a buoyant flow fueled by multiple rivers. Satellite observations during the October-November 2019 study period indicate the ICC often separates from the southwest tip of the Reykjanes Peninsula; it subsequently has large offshore excursion during west-southwestward winds. Results from a high-resolution realistic simulation exhibit this ICC behavior and provide detail on the associated currents and salinities. Sensitivity tests with simplified bathymetry, no winds, or no local buoyancy inputs are compared to the standard run to isolate contributions of those factors to flow separation. Analysis indicates that ICC separation occurs because the coast turns more tightly than the inertial radius; this behavior is consistent with inviscid theory. Partial flow deflection over the shelf expression of the Reykjanes Ridge and the widening shelf both increase ICC offshore excursion. The ICC is strongly influenced by the barotropic wind response to west-southwestward winds that includes a downshelf jet (flowing in the direction of Kelvin wave propagation) along the coast upshelf of the peninsula's tip where winds are downwelling-favorable, the downshelf extension of the jet that bends around the peninsula and progresses farther offshore with isobaths, a band of offshore and upshelf currents along the coast downshelf of the peninsula's tip, and surface flow aligned with Ekman transport located offshore beyond the downshelf jet. Similar wind-influence scenarios are discussed for other plumes. There are likely many such hotspots for offshore freshwater transport around the world.

Keywords

Iceland, river plume, freshwater, peninsula, coast, separation, bathymetry, winds

1 Introduction

Rivers supply the coastal ocean with buoyant waters that are laden with terrestrial materials (Milliman and Farnsworth, 2013). Riverine freshwater can change ocean water properties, increase vertical stratification, and introduce nutrients, sediments, and pollutants on continental shelves (Meybeck, 2003). The manifold effects of river plumes include influencing ocean dynamics, biogeochemistry, ecosystems, and fisheries (e.g. Dittmar and Kattner, 2003; Hickey, et al., 2010; Grimes, 2001). River plume dynamics are among the shelf transport mechanisms that exert strong control on nutrient distributions, productivity, and higher trophic levels (Stock et al., 2017). Fully describing riverine freshwater influences in the marine environment requires consideration of the wide variety of factors affecting the mixing and transport of river plumes. While many scenarios have been studied, there are many other situations influencing buoyant river plumes in nature that still need attention. Buoyant dynamics, coastal and bathymetric interactions, and wind forcing can combine in a complex variety of scenarios. Situations where buoyant waters are transported offshore and mixed with ambient shelf waters help inform the understanding of shelf exchange, "arguably the central problem in coastal physical oceanography" (Brink, 2016).

Several research reviews summarize the extensive body of research on river plumes (O'Donnell, 2010; Chant, 2011; Hetland and Hsu, 2013, Horner-Devine et al., 2015). Garvine (1995) classifies buoyant outflows as small-scale to large-scale plumes in order of increasing Kelvin number, the ratio of plume width to the internal Rossby radius. The large-scale plumes have a geostrophic across-shelf momentum balance and tend to form slender coastal currents stretching far downshelf (in the direction of Kelvin wave propagation) while under buoyancy-driven conditions (Garvine, 1995). Buoyancy-driven large-scale plumes are further categorized as surface-advected plumes or bottom-advected plumes (Yankovsky and Chapman, 1997). The transport and features of such plumes are described in terms of theory and idealized modeling by Yankovsky and Chapman (1997).

As buoyant plumes travel downshelf, they can encounter coastal features such as peninsulas, headlands, embayments, and curving coastlines. Plume interactions with tightly turning coasts can lead to flow separation, gyre and bulge formation, increased across-shelf transport, eddy generation, and mixing of buoyant waters (Bormans and Garrett 1989; Klinger 1994; Cenedese and Whitehead, 2000; Horner-Devine et al., 2006). Plumes that extensively interact with the bottom can experience separation from isobaths analogous to coastal separation than can be described with inviscid dynamics (Jiang, 1995; Garrett, 1995). Alternately, frictional adjustment in the presence of a downshelf background flow can keep the foot of a large-scale buoyant plume attached to a particular isobath, even as the bathymetry curves tightly around headlands and other features (Brink, 1998; Yankovsky and Chapman, 1997; Chapman, 2003). Bottom interactions and slope-control are stronger in shallow waters of more gently sloping shelves (Lentz and Helfrich, 2002).

Winds can reshape plumes and generate strong mixing. Buoyant waters can be advected by surface Ekman transport. Plume stratification tends to compress the surface Ekman layer, such that associated velocities are intensified and the deep-water Ekman solution applies in shallower waters closer to the coast (McWilliams et al., 2009; Moffat and Lentz, 2012; Chen et al., 2019). Upwelling-favorable winds can drive offshore transport in the surface Ekman layer and lead to rapid mixing with ambient shelf waters (Fong and Geyer, 2001; Lentz, 2004). In contrast, downwelling-favorable winds often confine plumes close to the coast, increase bottom contact via mixing and isopycnal steepening (Moffat and Lentz, 2012). Winds also can drive geostrophic alongshelf currents that affect the alongshelf distribution of plume waters. Upwelling-favorable winds can slow or reverse large-scale plumes, while downwelling-favorable winds can increase the downshelf transport and plume extent (Whitney and Garvine, 2005; Moffat and Lentz, 2012). Such wind-generated alongshelf currents can extend downshelf far beyond the windy region; remote wind influences including coastally trapped waves can be comparable to local wind effects on alongshelf flow (e.g. Battisti and Hickey, 1984; Davis and Bogden, 1989; Griffin and Middleton, 1991; Pringle, 2002; Yang and Chen, 2021). Offshore and onshore winds, though less studied, also influence the structure and transport of river plumes (e.g. Hunter et al., 2010; Jurisa and Chant, 2013; Osadchiev and Zavialov, 2013; Mendes et al., 2014). For instance, offshore winds can advect plume waters offshore (e.g. Jurisa and Chant, 2013; Osadchiev and Zavialov, 2013).

This paper focuses on the separation of the Icelandic Coastal Current (ICC) from the tip of the Reykjanes Peninsula, in southwest Iceland. Large-scale river plumes emanating from the Þjórsá, Ölfusá, and other rivers fuel the ICC (e.g. Vilhjálmsson, 2002; Logemann et al., 2013), which itself can be considered to be a large-scale river plume. Ocean color satellite imagery likely shows sediment-laden river plume waters flowing along Reykjanes Peninsula's south coast, shooting past the end of the peninsula, and then continuing approximately northwestward offshore as the plume widens (Figure 1). The coinciding winds are west-southwestward, which drive north-northwestward Ekman transport. These winds are downwelling-favorable and offshore along the peninsula's south coast and upwelling-favorable and offshore along the nearly perpendicular west coast at the end of the peninsula. The

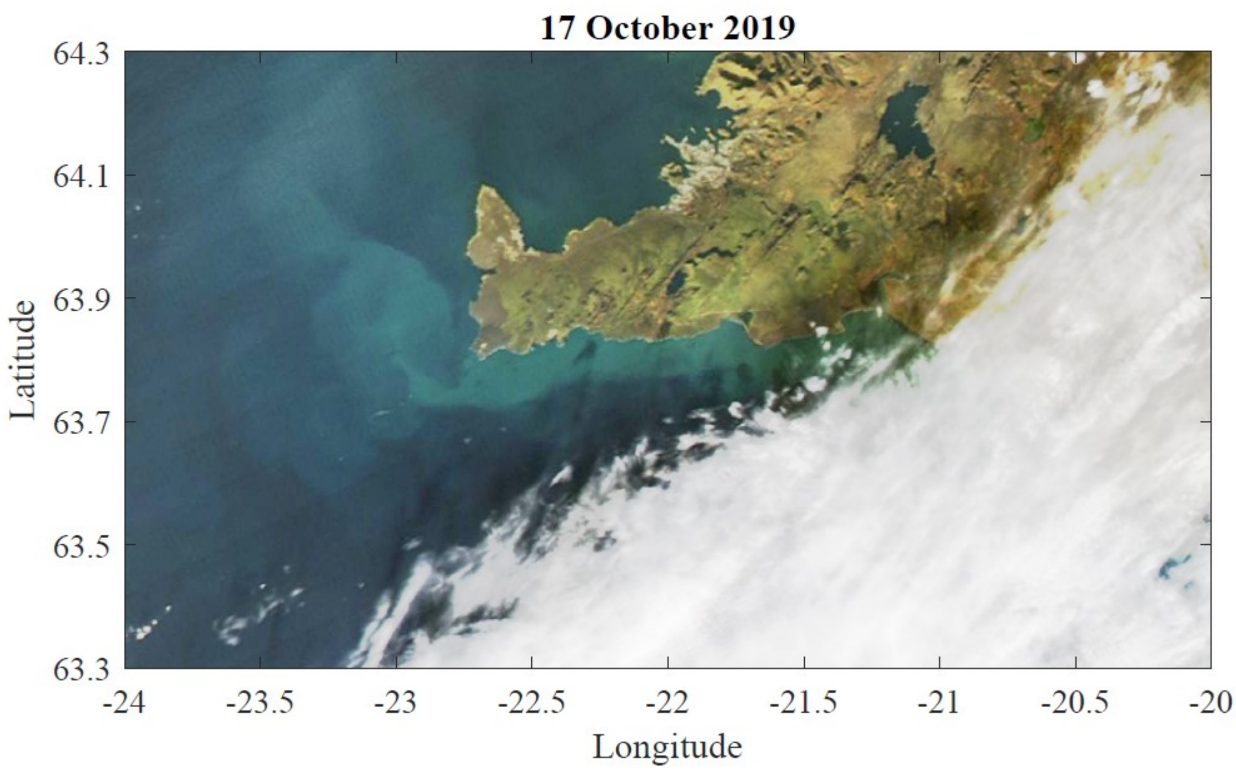

Figure 1 True-color satellite image on 17 October 2019 during 0.1 Pa west-southwestward winds. Lighter color waters likely are associated with sediment-laden ICC waters. The ICC apparently separates from Reykjanes Peninsula and progresses offshore under these conditions.

situation illustrates how a given wind direction can create qualitatively different situations for perpendicular peninsula coasts and other areas where coastline orientation abruptly changes (e.g. Alvarez et al., 2011; Camerlengo and Demmler, 1997; Reyes-Mendoza et al., 2016). The main objective of this study is describing and diagnosing the ICC separation from the southwest tip of the Reykjanes Peninsula and the subsequent offshore excursion. Particular attention is paid to the interplay of coastal curvature, bathymetry, and winds. Motivated by observations (e.g. Figure 1), realistic high-resolution (eddy-resolving) numerical simulations are conducted and analyzed. Sensitivity model runs for the study area are compared to isolate bathymetric and wind influences. Results are analyzed in the context of river plume theory and scalings. The discussion includes extension to other areas and overall relevance to offshore transport and exchange on continental shelves.

2 Study Area

Iceland is situated in the middle of a complex ocean current region with warm-water currents from the Atlantic and cold-water currents from the Arctic Ocean. The major surface currents that most influence the Icelandic shelf and slope regions are the Irminger Current, East Icelandic Current, North Atlantic Drift, and the South Icelandic Current (Logemann et al., 2013; Figure 2). The continental shelf varies from <10 km wide in several areas to >100 km in others (Figure 2). Iceland's terrestrial freshwater is delivered to the coastal ocean by a variety of glacially fed, direct runoff, and predominantly groundwater supplied rivers (Jonsdóttir, 2008).

The ICC is a buoyant shelf flow fueled by riverine freshwater inputs (Vilhjálmsson, 2002). The buoyant coastal current is shown as anticyclonically circulating around the entire Icelandic shelf in many studies (e.g. Stefánsson and Ólafsson, 1991; Vilhjálmsson, 2002; Loughlin et al., 2021), but it is most robustly identified as a continuous current only along the western side of Iceland (Malmberg and Kristmannsson, 1992; Logemann et al., 2013). The ICC region can be reliably tracked as a continuous downshelf current from its source region on the southwest Icelandic coast to the Vestfirðir (Westfjords) region. It can flow along or past the Reykjanes and Snæfellsnes Peninsulas and into or pass by Faxaflói, the large open bay between the two peninsulas (Figure 2). The ICC is around 10-20 km wide and 10-50 m thick with velocities exceeding 0.2 m/s and salinity anomalies around one in the vicinity of Faxaflói (Ólafsson et al., 2008; Logemann et al., 2013; Lin et al., 2020; MFRI Cruise Reports). In the Denmark Strait around the Westfjords region, ICC waters mix with the North Icelandic Irminger Current, which flows along the shelf-slope boundary in the same direction as downshelf flows (Logemann et al., 2013). This pathway is an important route for delivering riverine freshwater to the open ocean.

The present study focuses on southwest Iceland, where the ICC is fed by the Þjórsá, Ölfusá, and other rivers and the combined large-scale buoyant plume interacts with the Reykjanes Peninsula (Figure 2). The Þjórsá and Ölfusá Rivers are the two largest rivers in southwest Iceland; each has annual freshwater discharge around 400 m^3/s. The Ölfusá mouth is situated at a coastal bend at the start of the Reykjanes Peninsula, which stretches 74 km downshelf to its tip. The Þjórsá enters 23 km upshelf (opposite the direction of Kelvin wave propagation) of the Ölfusá on a 70 km stretch of straight coastline (Figure 2). The Rangá and Markarfljót are smaller rivers with river mouths 36 km and 71 km upshelf of the Ölfusá mouth. These smaller rivers collectively have smaller annual discharge than either the Þjórsá or Ölfusá. Iceland's Marine & Freshwater Research Institute (MFRI) seasonally surveys ocean and coastal hydrography around Iceland. The only regularly repeated transect in this study's southwest Iceland focus area crosses the shelf near the Rangá mouth; it is the Selvogsbanki transect. A buoyant river plume is present for 71% of the seasonal transects from 1997-2020; the average plume width (W) is 19 km and the average maximum plume thickness (h) is 46 m (MFRI Cruise Reports). The average density anomaly ($\Delta\rho$) associated with the maximum salinity contrast across the transect is 1.1 kg/m^3 and the corresponding reduced gravity ($g'=g\Delta\rho/\rho_o$, with gravitational acceleration g and reference density ρ_o) is 0.009 m/s^2 (MFRI Cruise Reports). The corresponding scale for the first-mode internal wave speed ($c_s=\sqrt{g'h}$) is 0.64 m/s. The internal Rossby (or deformation) radius ($R=c_s/f$, with Coriolis parameter f =1.31x10^{-4} s^{-1} for 63.8 °N latitude) is 5 km, and the Kelvin number ($K=W/R$) of 4 indicates a large-scale plume. The ICC at the observed transect has freshwaters from the Rangá, Markarfljót, and perhaps from rivers farther upshelf.

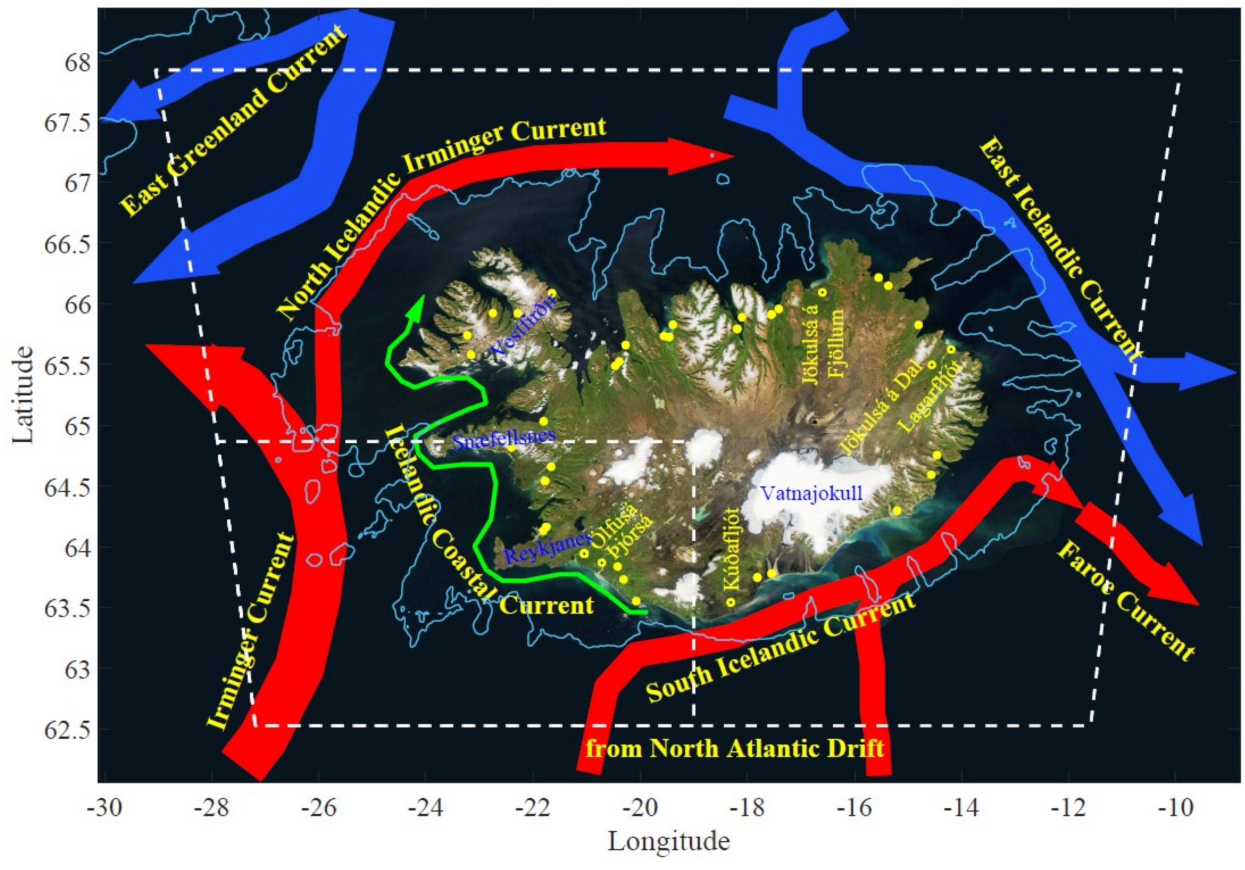

Figure 2 Iceland study area. Warm (red) and cool (blue) ocean currents are sketched along with the approximate ICC path (green), after Figure 8 in Logemann et al. (2013). Outer and inner southwest Iceland grid boundaries (dashed white), 200 m isobath (blue contour line), major river names (yellow), river gauge locations (yellow dots), and other place names (blue) are superimposed. Background is a true-color satellite image (from 14 August 2020) on a nearly cloud-free day over Iceland; clouds offshore of the shelf have been masked out.

The Þjórsá and Ölfusá add much more freshwater to the ICC. The 2019 ocean color observations (Figure 1) indicate the sediment-laden plume is 6-12 km wide along the south coast of the Reykjanes Peninsula during downwelling-favorable winds.

The relatively large observed plume thickness (h~50 m) indicates the ICC interacts with shelf bathymetry and should be categorized as a bottom-advected plume on average. Average shelf slopes (α) out to the 100 m isobath are relatively gentle ($0.001 \leq \alpha \leq 0.01$) upshelf of the Reykjanes Peninsula and moderate (α=0.004) at the Selvogsbanki observational transect. Slopes steepen downshelf from 0.01 to 0.04 along the peninsula's south coast and flatten out to 0.005 along the peninsula's west coast (Figure 2). The squared ratio of bottom slope to isopycnal slope (scaled as h/R) is the slope Burger number defined as $B_\alpha = (\alpha R/h)^2$ (Mysak, 1980; MacCready and Rhines, 1993), which is consistent with the original definition (Burger, 1958; Phillips, 1963; Ball, 1965). Note that the slope Burger number alternately can be defined as $\alpha R/h$ (Ou, 1980; Lentz and Helfrich, 2002); both definitions continue to be used. B_α=0.2 over the moderately sloped observational transect, $B_\alpha \geq 1$ for the steeper slopes along the peninsula's south coast, and B_α reduces to 0.3 along the peninsula's west coast. The Reykjanes Ridge (Figure 2) extends southwest from the peninsula's tip with steep bathymetry and outcrops on the shelf (known as the Fuglasker), with which the ICC may interact.

3 Methods

Satellite images (e.g. Figure 1) are derived from Moderate Resolution Imaging Spectroradiometer (MODIS) corrected reflectance imagery available from NASA Worldview (https://worldview.earthdata.nasa.gov/). MODIS data from the Aqua satellite are used. The true-color images use MODIS bands 1, 3, and 4 and are sharpened to 250 m resolution. After downloading images from NASA Worldview, the images are brightened following a method similar to Fanning (2009). With the applied brightening method, the 0-255 range on the red-green-blue (RGB) color scale are remapped from [0, 10, 100, 255] to [0, 10, 200, 255] and linearly interpolated between each breakpoint. Representative images with breaks in cloud cover and the sediment-laden plumes consistent with the ICC in the southwest Iceland study area are included for the October-November 2019 study period. Most analysis focuses on images from 17 October and 25 November 2019. Supplementary analysis includes images from 06, 18, and 26 October and 13, 14, and 26 November 2019. Selecting the late fall study period avoids potentially confusing phytoplankton blooms with river plumes since blooms are less likely to occur in this season.

The Regional Ocean Modeling System (ROMS, Haidvogel et al., 2000; Haidvogel et al., 2008) is applied to model coastal and open ocean waters around Iceland. ROMS is a free-surface, hydrostatic, primitive-equation model that evolves the governing momentum, mass, and tracer conservation equations in finite-differenced form. The advection schemes used are 3rd-order upstream for 3D momentum, 4th-order centered for 2D (depth-averaged) and vertical momentum, and the Wu and Zhu (2010) 3rd-order scheme for salinity and temperature. Vertical turbulent viscosity and diffusivity are parameterized with the generic length scale method k-epsilon closure scheme. Salinity is calculated with the Practical Salinity Scale, so reported salinities are dimensionless.

For the Iceland model runs, the outer (mother) grid domain spans 800x600 km at 4 km (eddy-permitting) horizontal resolution and includes Iceland's entire continental shelf and surrounding open ocean waters (Figure 2). The nested inner grid for southwest Iceland covers 422.4x262.4 km at 0.8 km (eddy-resolving) maximum horizontal resolution (Figure 2 and Figure 3). The inner grid has offshore transition zones where boundary-parallel resolution is stepped up from 4 km to 1.6 km before reaching the 0.8 maximum resolution; these zones span 138.4 and 42.4 km inward from the west and south offshore boundaries, respectively. Vertical resolution in both grids is supplied by 30 evenly distributed sigma levels. Model bathymetry for both grids is interpolated from the 1 arc-minute ETOPO1 Global Relief Model (Amante and Eakins, 2009). The Coriolis parameter varies with latitude as in nature. The model is initialized with surface elevations, subtidal velocities, temperatures, and salinities interpolated from the Hybrid

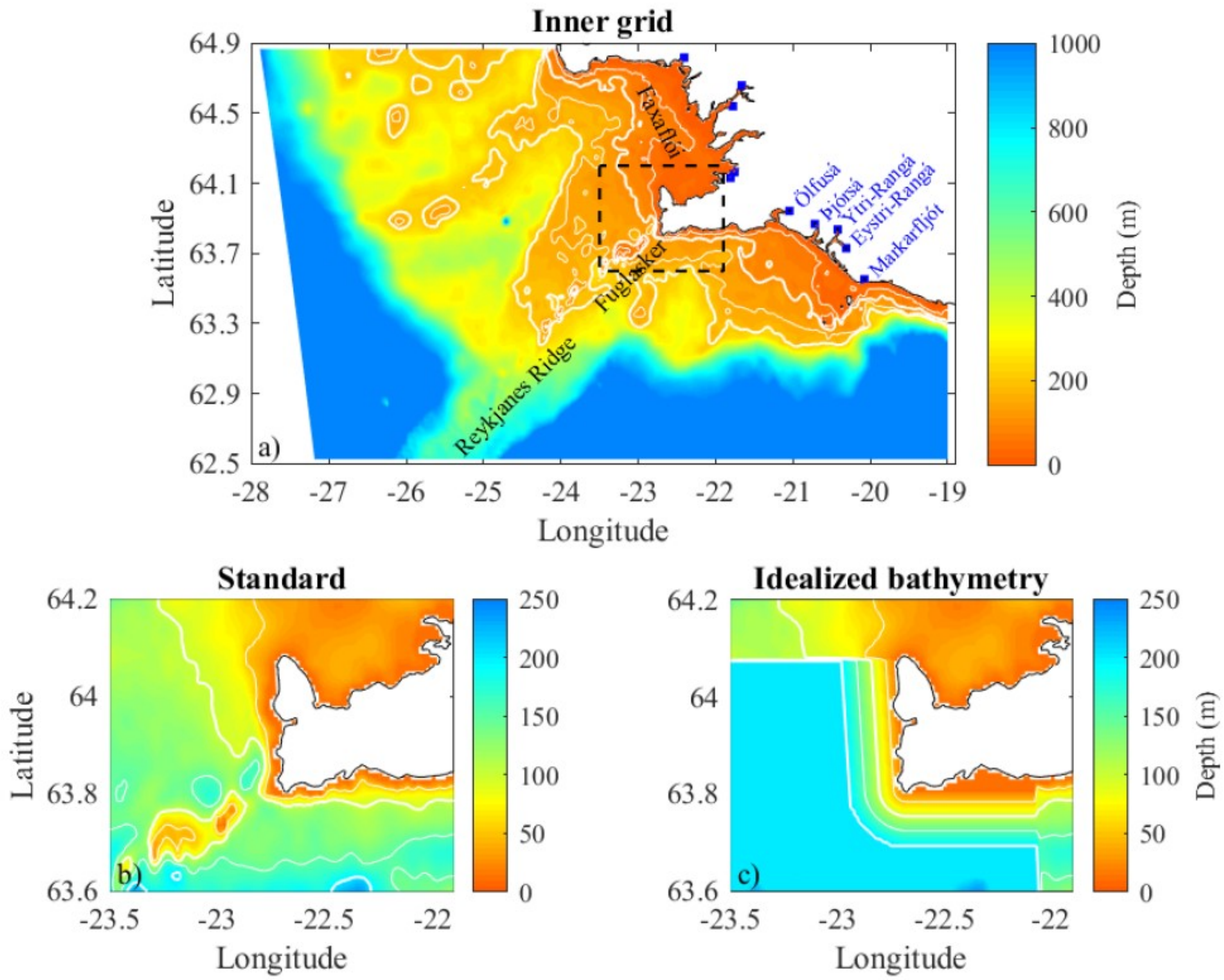

Figure 3 Model bathymetry for a) the entire inner grid for southwest Iceland, b) a close-up around the Reykjanes Peninsula for the standard configuration, and c) a close-up for the sensitivity test with idealized bathymetry. River inputs are marked (blue), rivers upshelf of the Reykjanes Peninsula are labeled (blue), and ocean place names are labeled (black) on the upper panel.

Coordinate Ocean Model (HYCOM, Chassignet et al., 2007); specifically, the Global Ocean Forecasting System 3.1 output on the 0.04° latitude 0.08° longitude grid is used. The outer model is forced along the open ocean boundaries with the semi-diurnal lunar (M_2) tidal constituent from the OSU TOPEX/Poseidon Global Inverse Solution (Egbert and Erofeeva, 2002) and subtidal velocities, temperatures, and salinities from HYCOM. The major axis of M_2 tidal currents, as represented in the OSU TOPEX/Poseidon Global Inverse Solution, are generally aligned locally alongshelf and are strongest (0.3-0.5 m/s) around the Westfjords region and the Iceland-Faroe Ridge (extending southeastward from Iceland). Tidal current amplitudes are 0.1-0.3 m/s in the vicinity of Reykjanes Peninsula, with the strongest currents around the peninsula tip. The initial and boundary information from HYCOM allows for the inclusion of ocean currents flowing through the area, temperature and salinity differences associated with ocean water masses, and large-scale sea-level gradients. For the outer grid at the surface, the northern boundary (-2-7 °C, 32.5-34.8 salinity) is generally cooler and fresher than the southern boundary (7-11 °C, 35.0-35.2) over the October-November 2019 study period. The western (-2-11 °C, 33.6-35.1) and eastern (3-10 °C, 34.5-35.2) outer boundaries have overlapping temperature and salinity ranges with somewhat cooler fresher waters to the west. For the inner grid at the surface, the northern (7-10 °C, 34.9-35.2) and southern boundaries (7-11°C, 35.0-35.2) have similar temperature ranges and fresher waters to the north. The western (7-11 °C, 35.0-35.2) and eastern (8-11 °C, 35.0-35.3) inner boundaries have overlapping temperature ranges and the same salinity range with somewhat cooler fresher waters to the west. Chapman (1985) and Flather (1976) boundary conditions are applied for surface elevation and depth-averaged velocities along the open boundaries. Orlanski radiation (Orlanski, 1976) with nudging open boundary conditions are applied for depth-varying velocities, temperature, and salinity. Spatially and temporally varying surface forcing is interpolated from HYCOM daily averaged surface stress. Net surface heat fluxes are set to zero. River forcing for the Iceland model runs is derived from hydrological observations by the Icelandic Meteorological Office (2021). Daily time series for 44 downstream river discharge stations are used to create 36 individual river input points at their geographic mouth locations around Iceland. For each river, measured discharge is multiplied by the ratio of gauged area to its total watershed area to better represent inputs from the watershed. Daily river temperature time series are from 19 downstream river stations that measure water temperature. Temperatures for rivers without temperature observations are set from the nearest monitored river. River temperatures range between -1 and 10 °C around Iceland and between 4 and 10 °C in southwest Iceland during the October-November 2019 study period. River buoyancy is dominated by the salinity contrast, not the relatively small river-to-ocean temperature differences in the study area. Rivers are introduced in ROMS as mass inputs at their natural mouth locations with horizontal volume fluxes set by daily discharge, daily temperatures, and constant zero salinity. Freshwater discharges from the Markarfljót, Rangá (with the Ytri- and Eystri-Rangá branches), Þjórsá, and Ölfusá Rivers, which enter upshelf of the Reykjanes Peninsula, are shown in Figure 4a for the main study period.

An Iceland model run with only the outer grid is initialized with HYCOM fields on 01 January 2019 and spans all of 2019. The main southwest Iceland analysis run with both the outer and inner grids is initialized from the original run on 02 October 2019 and ends on 03 December 2019, spanning 62.1 days (120 M_2 tidal cycles). A comparison no-wind sensitivity test has wind stress set to zero and has all other settings the same as the main analysis run (Table 1). Another sensitivity run has no buoyant river plumes from local rivers (within the southwest Iceland grid). This modification is accomplished by setting river inflow salinity at 35 to remove the buoyancy of the inflowing water; all other settings are the same as the realistic run. In other sensitivity runs, bathymetry around the Reykjanes Peninsula is modified to an idealized shelf (Figure 3c). Along the south coast within 30 km from the peninsula and along the west coast of the peninsula, the shelf slope is set to 0.015 from 10 to 200 m. The idealized bathymetry wraps the slope radially around the southwest coastal corner to transition between the perpendicular shelves. Areas shallower than 200 m along the southwest-running Reykjanes Ridge are set to 200 m in the idealized bathymetry. Sensitivity runs with the patched-in idealized bathymetry include runs with and without winds (Table 1). Tidally averaged fields of temperature, salinity, and velocities (in ROMS averaged files) output every 24.84 hours (two M_2 tidal cycles) are analyzed. Data presented in each figure are included in the supporting dataset (Whitney, 2022).

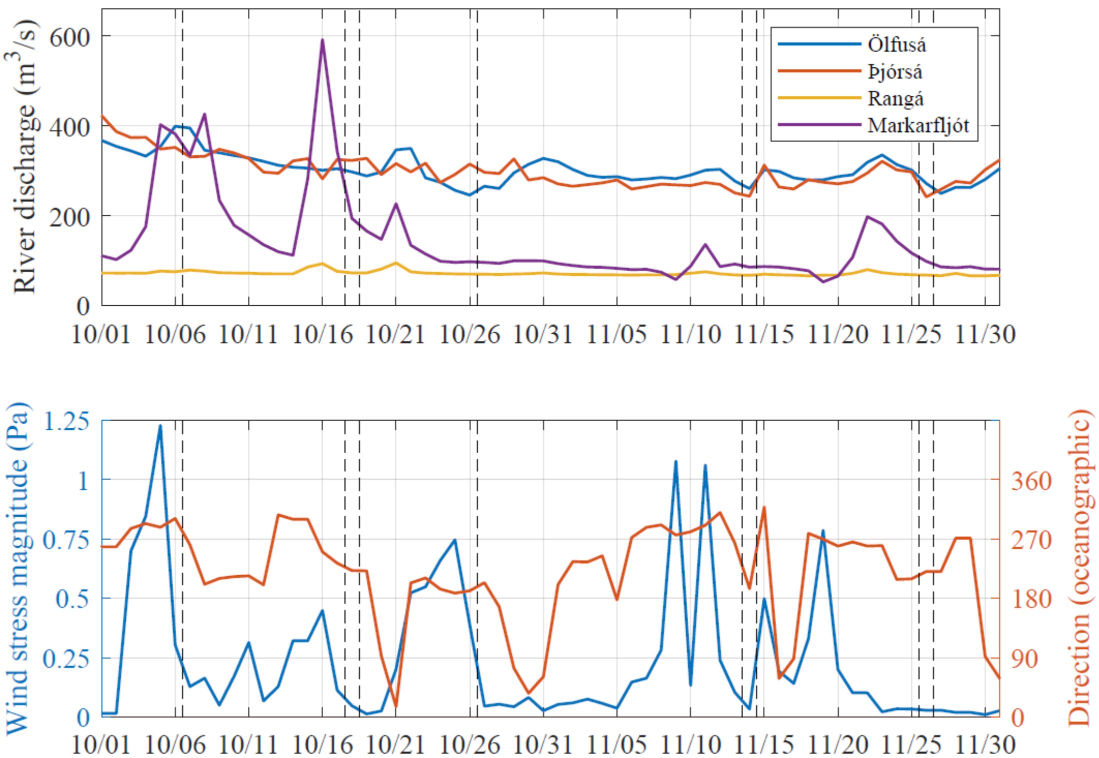

Figure 4 Model forcing time series for October-November 2019. a) Discharge for four rivers contributing to the ICC. b) Wind stress magnitude and direction averaged over Reykjanes Peninsula region. Vertical dashed black lines indicate the timing of satellite images included in this study.

Table 1 Model run descriptions. Many runs include observed (obs.) values for slope, freshwater discharge, and/or wind stress.

Name	Runs	r_c (km)	Slope	Tide	Fresh dis. (m^3/s)	Wind stress (Pa)	Wind dir. (°T)
Realistic (main analysis)	1	≤3	obs.	M_2	obs.	obs.	obs.
Sensitivity tests							
Idealized bathymetry	1	≤3	0.015	M_2	obs.	obs.	obs.
No wind	1	≤3	obs.	M_2	obs.	0	n/a
Ideal. bathy., no wind	1	≤3	0.015	M_2	obs.	obs.	obs.
No river plumes	1	≤3	obs.	M_2	0	obs.	obs.

4 Results and Analysis

4.1 Observations and realistic simulation

Throughout the October-November 2019 study period, the Ölfusá and Þjórsá discharges each range between 250-400 m^3/s (Figure 4a). The Markarfljót River is much more variable; with discharge ranging from the 600 m^3/s peak on 16 October 2019 down to 50 m^3/s in mid-November. The Rangá River has the smallest discharge and variability; it ranges between approximately 50-100 m^3/s during the study period. There are several strong wind events with peak daily wind stresses exceeding 0.2 Pa; the strongest wind event (in early October) peaks at 1.0 Pa (Figure 4b). Winds are predominantly southward to west-northwestward during the study period. During most events, winds tend to be closer to westward, which is downwelling-favorable along the south coast and directed offshore on the peninsula's west coast.

4.1.1 17 October 2019: west-southwestward winds

On 17 October 2019, when a satellite-observed sediment-laden plume is present (Figure 1), the Ölfusá and Þjórsá discharges each are 300-350 m^3/s, the Markarfljót is dropping from 350 to 200 m^3/s, and the Rangá is around 70 m^3/s (Figure 4a). The total freshwater discharge from these four rivers is approximately 1000 m^3/s on this date. The timing is towards the end of a 5-day wind event with peak 0.45 Pa winds. Wind stress is west-southwestward at 0.11 Pa on 17 October (Figure 4b). Specifically, the wind stress is directed towards 230-250 °T (degrees clockwise from true north) in the vicinity of the peninsula. Thus, winds are directed downshelf (downwelling-favorable) and offshore along the south coast and upshelf (upwelling-favorable) and offshore along the peninsula's west coast. The wind direction corresponds with a north-northwestward deep-water surface Ekman transport. The observed sediment-laden plume (Figure 1) has a roughly northwestward trajectory away from the peninsula tip. The plume widens from approximately 8 km wide while still attached to the coast to around 30 km after separation from the peninsula. The inner and outer edges of the plume are respectively 20 km and 50 km west of the northwest tip of the peninsula. Colors in the satellite image suggest there are more-dispersed lower-concentration coastal waters farther offshore.

Model results for the same day indicate the observed sediment-laden plume is consistent with the pathway of the ICC and its contributing river plumes. The model surface salinity field (Figure 5) shows each river plume spreading outward from the river mouths and downshelf along the south coast within the ICC. Salinity anomalies are calculated as $\Delta S = S_o - S$ with S_o=35.2; the reference salinity is representative of southern offshore waters and the same value is applied for “pure Atlantic Water” in Logemann et al. (2013). Anomalies are 2-7 outside the river mouths, with the largest ΔS at the Ölfusá mouth. The ΔS approximately exponentially decreases downshelf from the Ölfusá mouth with an e-folding length scale of around 15 km. The maximum ΔS is near 0.2 for the 30 km closest to the peninsula tip. The cross-shelf section representative of conditions along the peninsula’s south coast (Figure 6a) indicates there is an inner low-salinity plume, with W=7 km and h=50 m, composed of newly introduced river waters contained within the broader ICC, which has an overall weaker salinity anomaly and extends at least 18 km offshore at the surface and out to the 130 m isobath. The inner low-salinity plume and the overall ICC can be characterized as a large-scale bottom-advected plume under downwelling conditions at this time. The core of the downshelf flow is centered 2-8 km offshore (between the 50-100 m isobaths) along most of the peninsula’s south coast (Figure 5). Surface speeds in the core are 0.8-1.2 m/s; the cross-section (Figure 6a) indicates the strongest velocities (≥0.7 m/s) are contained with the upper 10 m. The wider deeper jet, with velocities ≥0.2 m/s, extends down to the 110 m isobath. Core subtidal velocities are many times larger than M_2 tidal currents (0.1 m/s) in the area; consequently, the ICC does not experience tidal reversals in this area during these conditions.

Modeled conditions on the peninsula’s south coast at the selected cross-section (Figure 6a, where α=0.02) can be expressed in terms of relevant velocity, width, and slope scales. The inner

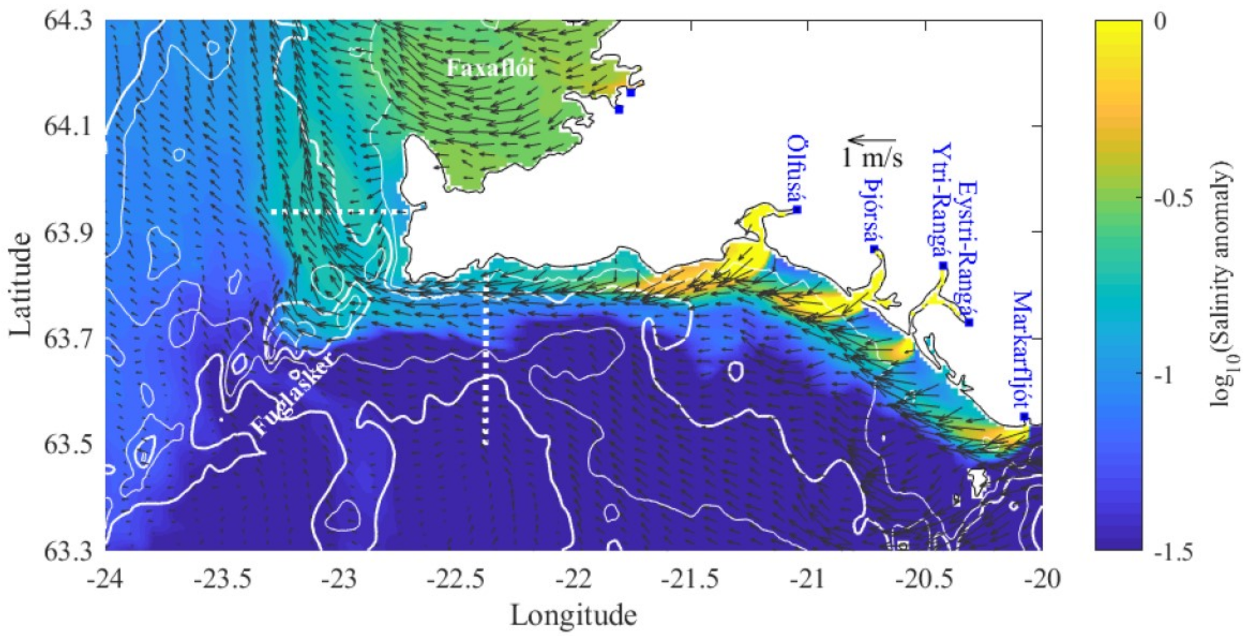

Figure 5 Surface salinity anomalies (shaded) and velocities (arrows) on 17 October 2019. Velocity vectors are subsampled to respectively show every sixth and third data point along east-west and north-south grid lines. The 50, 100, 150, and 200 m isobaths (white contours) and cross-section positions (white dashed) are shown. River inputs are marked (blue), rivers upshelf of the Reykjanes Peninsula are labeled (blue), and ocean place names are labeled (black).

low-salinity plume (with g'=0.002 m/s^2, h=50 m, and W=7 km) has c_s=0.32 m/s, R=2.4 km, K=3, and B_α=0.9. The broader ICC (with g'=0.001 m/s^2, h=130 m, and W=18 km) has c_s=0.36 m/s, R=2.8 km, K=6, and B_α=0.2. The B_α values indicate this in an intermediate situation that is between the vertical-wall limit ($B_\alpha \to \infty$) with no bottom interaction and the gentle-slope limit ($B_\alpha \to 0$) with extensive slope-control (Lentz and Helfrich, 2002). Thermal-wind balance indicates buoyancy-driven alongshelf flow (u_{buoy}) should scale as c_s, even for plumes interacting with sloping shelves (Yankovsky and Chapman, 1997; Lentz and Helfrich, 2002). The downwelling-favorable winds should add to the downshelf flow. A steady barotropic wind response is governed by a depth-integrated alongshelf momentum balance between wind stress (τ_{sx}) and bottom stress. The associated scale for the depth-averaged wind-driven alongshelf flow is $u_{wind} = \sqrt{\tau_{sx}/(\rho_o C_{Da})}$ for quadratic drag (where C_{Da} is the drag coefficient appropriate for depth-averaged velocities) (Whitney and Garvine, 2005). The along-shelf plume velocity (u_p) is approximately the sum of the buoyancy-driven and wind-driven contributions: u_p=u_{buoy}+u_{wind} (Whitney and Garvine, 2005; Lentz and Largier, 2006; Moffat and Lentz, 2012). For 0.09 Pa alongshelf wind stress and quadratic drag with C_{Da}=0.002, u_{wind}=0.21 m/s. For the c_s values calculated above, the u_p scale is approximately 0.5-0.6 m/s for the downwelling conditions on 17 October. The u_p scale is consistent with depth-averaged velocities within the ICC, which peak at 0.6 m/s in the inner plume (Figure 6a). A non-dimensional wind strength index (W_s) for plumes rates the

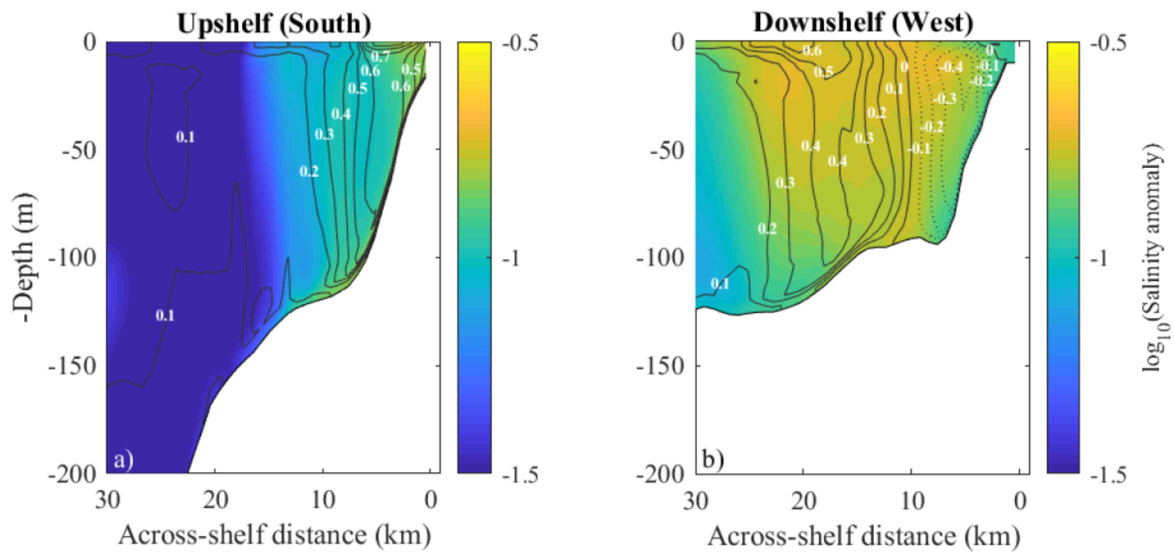

Figure 6 Salinity anomalies (shaded) and local alongshelf currents (solid and dashed lines for downshelf and upshelf flow, respectively) for 17 October 2019 at cross-shelf sections at 15 km a) upshelf or b) downshelf of Reykjanes Peninsula's southwest tip. Section locations are shown in Figure 5. Velocity contours have a 0.1 m/s interval and are labeled in white.

importance of wind-driven flow relative to buoyancy-driven flow: W_s=u_{wind}/u_{buoy} (Whitney and Garvine, 2005). W_s=0.7 at this time, indicating a strongly wind-influenced plume where wind-driven and buoyancy-driven flow components have similar magnitudes. Winds were much stronger on the previous day and W_s exceeds one, indicating a previously wind-dominated plume.

The ICC separates from the southwest tip of the peninsula, then turns to flow northwestward, and the jet center is 22 km offshore by the northwest tip of the peninsula (Figure 5). Core surface velocities decrease from 1.0 m/s to 0.6 m/s as the ICC flows offshore. These core velocities are two to three times the M_2 tidal current amplitudes (0.2-0.3 m/s) in the area. The orientation range of the core surface currents is 300-355 °T, with currents tending to shift more northwards farther downstream after separation. Inshore of the ICC, surface currents have upshelf (southward) and offshore (westward) components along the peninsula's west coast. Part of the ICC deflects over the shallow Fuglasker (part of the Reykjanes Ridge) close to the peninsula's southwest tip and then rejoins the main current farther downstream. Maximum surface salinity anomalies are around 0.2 after coastal separation. The low-salinity region (with $\Delta S \geq 0.10$) associated with the main ICC flow is much wider ($15 \leq W \leq 30$ km) after separation than it is along the peninsula's south coast. More diffuse ICC waters (with $0.05 \leq \Delta S < 0.10$ and slower currents) extend much farther offshore (at least out to the 150 m isobath), similar to the diffuse coastal waters observed in the satellite image. Analysis of the sequence of model results leading up to this time, indicates ICC waters were delivered to the shelf, transported, and mixed over the prior weeks and months. These older diffuse ICC waters are not part of the new plume waters actively advancing around the peninsula. Note that there also is low salinity within Faxaflói; analysis of preceding model results indicates this freshwater comes from river sources within the bay and river waters transported downshelf and into the bay by the ICC at earlier times. The east-west oriented cross-shelf section at the middle of the peninsula's west coast cuts obliquely across the ICC and indicates conditions after separation (Figure 6b). Salinity anomalies increase towards the surface, but span the entire water column over a large area out to the 125 m isobath. Isohalines are oppositely sloped on the offshore and inshore sides of the plume. The northwestward flow of the ICC extends throughout the water column and is centered near-surface at 20 km offshore. Near-bottom ICC velocities exceeding 0.2 m/s reach out to the 125 m isobath; this is the offshore foot of the plume at this section. The inshore southward counter flow extends out to 10 km offshore.

There are several dynamical reasons that possibly contribute to ICC separation from the southwest tip of the Reykjanes Peninsula. Guidance from inviscid theory suggests baroclinic flows can centrifugally separate where the coastal radius of curvature (r_c) is smaller than the inertial radius of the flow ($r_i = u_p/f$ for river plumes) (Bormans and Garrett, 1989; Klinger, 1994; Garrett, 1995). The ICC meets this inviscid criteria for coastal separation at the southwest tip of the peninsula since $r_c \leq 3$ km and $r_i = 5$ km for the 17 October conditions. The ICC speed and r_i are augmented by the downwelling-favorable winds along the peninsula's south coast. The ICC strongly interacts with the bottom, which suggests that isobaths may play an important role in guiding the flow. Inviscid baroclinic flows will centrifugally separate from an isobath under conditions similar to coastal separation (Jiang, 1995; Garrett, 1995). The ICC also meets the inviscid criteria for isobath separation since isobaths between 50-100 m turn at least as tightly as the coastline around the peninsula tip. After separation, an anticyclonic gyre (eddy) can form that is analogous to the bulge recirculation that buoyancy-driven plumes form outside river mouths when r_i is at least the scale of R (Horner-Devine et al., 2006). This eddy forming condition is met since $r_i > R$. The deflection around the Fuglasker may be partially due to this bulge-forming process.

Inviscid mechanisms, however, may not purely apply since bottom stress is relatively strong (0.02-0.20 Pa) along the ICC path, with the highest values at the peninsula's southwest tip. Another bathymetric mechanism, which is inherently frictional, tends to move the foot of large-scale buoyant flows out to a trapping isobath where bottom Ekman transport is arrested (Yankovsky and Chapman, 1997; Chapman, 2003). In the presence of a background downshelf flow, such as currents driven by downwelling-favorable winds, theory and idealized modeling indicate the foot of large-scale buoyant flows follows its trapping isobath, even where bathymetry curves tightly around headlands and other features (Brink, 1988; Chapman, 2003). The ICC does not exactly follow any isobaths around the peninsula, but the flow pathway falls within the general orientation range of the 100-130 m isobaths. The fact that the foot of the buoyant flow is mostly near the 130 m isobath within 15 km upshelf and downshelf of the peninsula's southwest tip suggests some bathymetric steering, but the foot shoals to the 100 m isobath farther downshelf. This steering mechanism may not apply for the ICC because even though winds drive the downshelf background flow necessary for this steering they also lead to bottom Ekman transport that prevents an arrested Ekman layer.

Advection by wind-driven currents is an important mechanism that may guide the plume offshore. The wind response is complex around the peninsula, but surface Ekman transport, remote effects extending downshelf, and local coastal wind-driven currents must be involved. The surface Ekman transport is north-northwestward, which is close to the northwestward ICC trajectory after separation from the peninsula. The Ekman depth ($h_e=\pi\sqrt{2A_z/f}$, with vertical eddy viscosity A_z) is ~10 m and the ICC extends much deeper, so it is unlikely that the ICC path is guided by surface Ekman transport only. Furthermore, the ICC surface currents are roughly double the theoretical Ekman current magnitude right at the surface ($u_{es}=\pi\sqrt{2}\tau_s/(\rho f h_e)$), which is 0.35 m/s. The downwelling-favorable winds along the upshelf coast generate a wind-driven (0.21 m/s) downshelf flow. This wind-driven downshelf jet likely extends downshelf around the peninsula and plays a role in guiding the plume. The path of the wind-driven jet will become clear through analysis of the sensitivity tests. This wind-driven jet definitely is at least 10 km offshore of the peninsula's west coast because of the coastal band of upshelf (southward) currents. The 0.2-0.4 m/s southward counter flow is consistent with the response to local upwelling-favorable winds. The wind stress component directed upshelf (southward) is 0.07 Pa and the corresponding estimate for wind-driven alongshelf flow is 0.18 m/s. The offshore wind and coastal flow components likely are linked. The local response to offshore winds has been shown to advect plume waters offshore in other areas (e.g. Jurisa and Chant, 2013; Osadchiev and Zavialov, 2013). How these elements of wind response combine will become more evident through analysis of the sensitivity tests.

4.1.2 25 November 2019: weak winds

The low-wind conditions on 25 November 2019, when sediment-laden ICC waters again are observed by satellite (Figure 7), provide a comparison for the 17 October 2019 situation. Wind stress is south-southwestward to west-southwestward (190-245 °T) at only 0.03 Pa and was equally weak over the two previous days (Figure 4b). The Ölfusá and Þjórsá discharges are both 300 m^3/s, the Markarfljót is near 120 m^3/s after its peak discharge, and the Rangá is 70 m^3/s. The total freshwater discharge from these four rivers is approximately 790 m^3/s on this date (Figure

4a). Color contrasts are weaker and colors are shifted towards green in the 25 November 2019 satellite-image (Figure 7) because of the dim sunlight as winter approaches; data farther north is blacked out due to even less available sunlight. The sediment-laden waters extend 6-17 km offshore along the peninsula's south coast, with the narrowest areas near the southwest tip. The bounds of the sediment-laden waters extend offshore over the shallow Fuglasker areas and over a broad (42-63 km wide) region offshore of the peninsula's west coast approximately out to the 150 m isobath. The color in this area is patchier offshore and it appears the sediment-laden waters may be more concentrated closer to the coast, but the low color contrast provides only limited information in this regard.

The satellite observations are broadly consistent with the regions influenced by ICC waters in the model on the same day. The band of lower surface salinities (Figure 8) along the peninsula's south coast extend as far offshore as the observed sediment-laden areas (Figure 7). Low surface salinities (with $\Delta S \geq 0.05$) associated with the ICC extend over the shallow Fuglasker areas and out to the 150 m isobath (Figure 8), which is 45-60 km offshore of the peninsula's west coast. Salinity is lower (with $\Delta S \geq 0.10$) close to the peninsula's west coast where the satellite observations suggest somewhat higher sediment concentrations. Salinity anomalies are 2-6

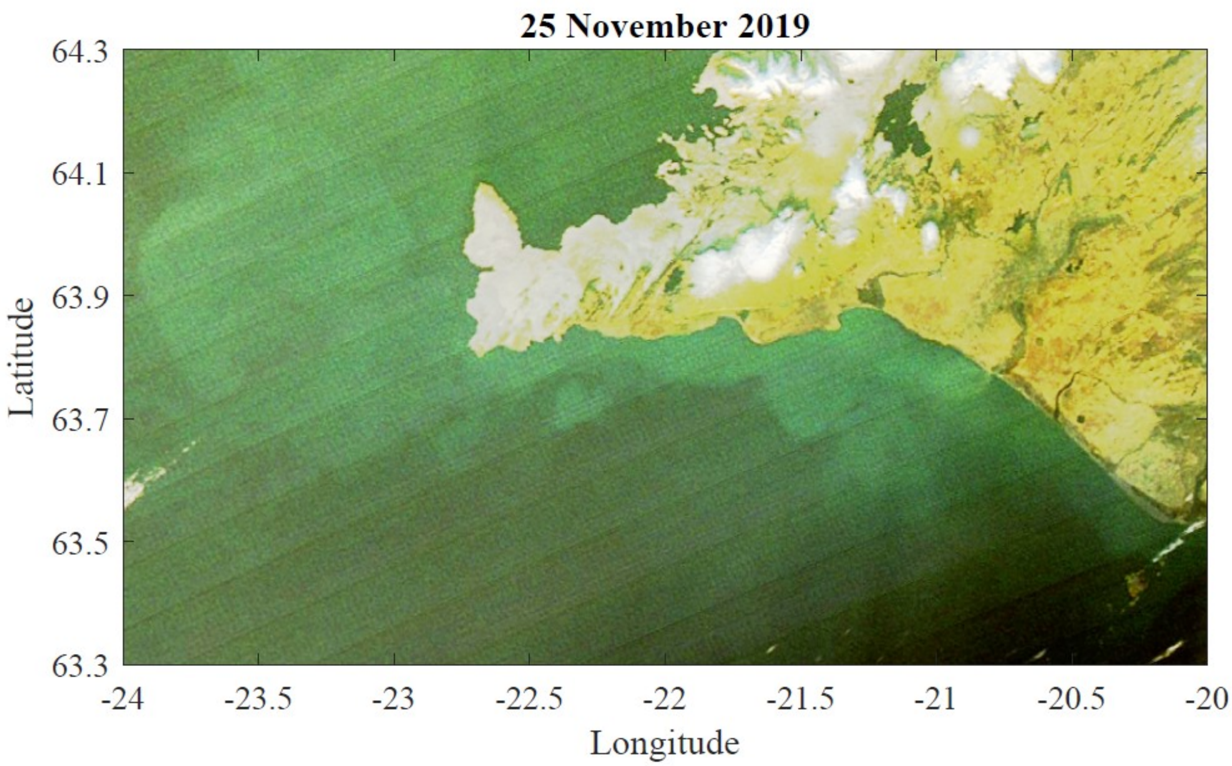

Figure 7 True-color satellite image on 25 November 2019 during light winds. Lighter color waters likely are associated with sediment-laden ICC waters. Greenish relatively low-contrast appearance of waters is associated with low incident light levels at high latitudes this time of year.

outside the river mouths, with the largest ΔS at the Ölfusá mouth. The maximum ΔS decreases from 2 at 10 km downshelf of the Ölfusá mouth to 0.3 near the peninsula's southwest tip. The salinity anomalies are stronger than during the downwelling conditions on 17 October 2019. The cross-shelf section for the peninsula's south coast (Figure 9a) again shows an inner area of low-salinity new plume waters (with maximum ΔS=0.40, W=7 km, and h=30 m) within the broader deeper ICC waters (with $\Delta S \geq 0.05$, W=16 km, and h=120 m). Even under these relatively low wind conditions, the inner plume and overall ICC strongly interact with the bottom; though the plume is somewhat shallower than during downwelling-favorable conditions. Surface speeds in the core of the downshelf flow weaken from 0.5 m/s to 0.3 m/s along the peninsula's south coast. Speeds are considerably slower than during strong downwelling winds, but remain stronger than M_2 tidal currents. The downshelf cross-section (Figure 9a) indicates the strongest velocities are in the upper 5 m and the wider deeper jet extends down to the bottom. At the cross-section, scales for the inner low-salinity plume (with g'=0.003 m/s^2) are c_s=0.30 m/s, R=2.3 km, K=3, and B_α=2.4. The scales corresponding to the broader ICC (with g'=0.0015 m/s^2) are c_s=0.42 m/s, R=3.2 km, K=5, and B_α=0.3. The B_α values are intermediate, but the higher values relative to downwelling conditions indicate somewhat reduced bottom interaction. The alongshelf wind stress component is at most 0.02 Pa, so $u_{wind} \leq 0.10$ m/s and $W_s \leq 0.3$. The corresponding u_p scales for the inner low-salinity plume and the overall ICC are at most 0.4-0.5 m/s. Both the velocity scales and model results indicate the ICC is slower under these weak-wind conditions than during stronger downwelling-favorable wind forcing.

Unlike during strong west-southwestward winds, the ICC turns relatively tightly around the peninsula's southwest tip and remains much closer to the west coast on 25 November 2019 (Figure 8). Part of the ICC flow, however, deflects around the Fuglasker and rejoins the rest of the current again. The center of the ICC velocity core most closely follows the 80 m isobath, which gradually moves offshore of the peninsula's west coast. Maximum core velocities decrease from 0.4 to 0.2 m/s along the current path and maximum ΔS remains near 0.20. Subtidal velocities remain larger than M_2 tidal current amplitudes as the ICC progresses around the peninsula. The orientation range of the core surface currents is 310-360 °T. Surface currents are somewhat more northward than during 17 October 2019, but the main difference is the ICC pathway is much closer to shore along the peninsula's west coast during the weak winds on 25 November 2019. The corresponding cross-section (Figure 9b) indicates the fastest flows are in the upper 10 m. Currents exceeding 0.1 m/s extend through the water column within the narrow (3 km) jet that extends out to the 80 m isobath. Isohalines slope offshore upwards from the foot of the plume, similar to the earlier strong-wind situation. There is a narrow (1-2 km) region of southward counter flow (at 0.1-0.2 m/s) along the southern half of the peninsula's west coast (Figure 8); the southward flow is narrower and slower than for the stronger west-southwestward wind situation (Figure 5). The main northward ICC region (with stronger currents and $\Delta S \geq 0.10$) extends 13-31 km offshore, and is wider farther north (Figure 8). Lower velocity and more diffuse freshwaters (with $0.05 \leq \Delta S < 0.10$) are present out to 45-60 km offshore, similar to the extent on 17 October 2019. As before, these are older diffuse ICC waters that are not part of the new active plume advancing around the peninsula.

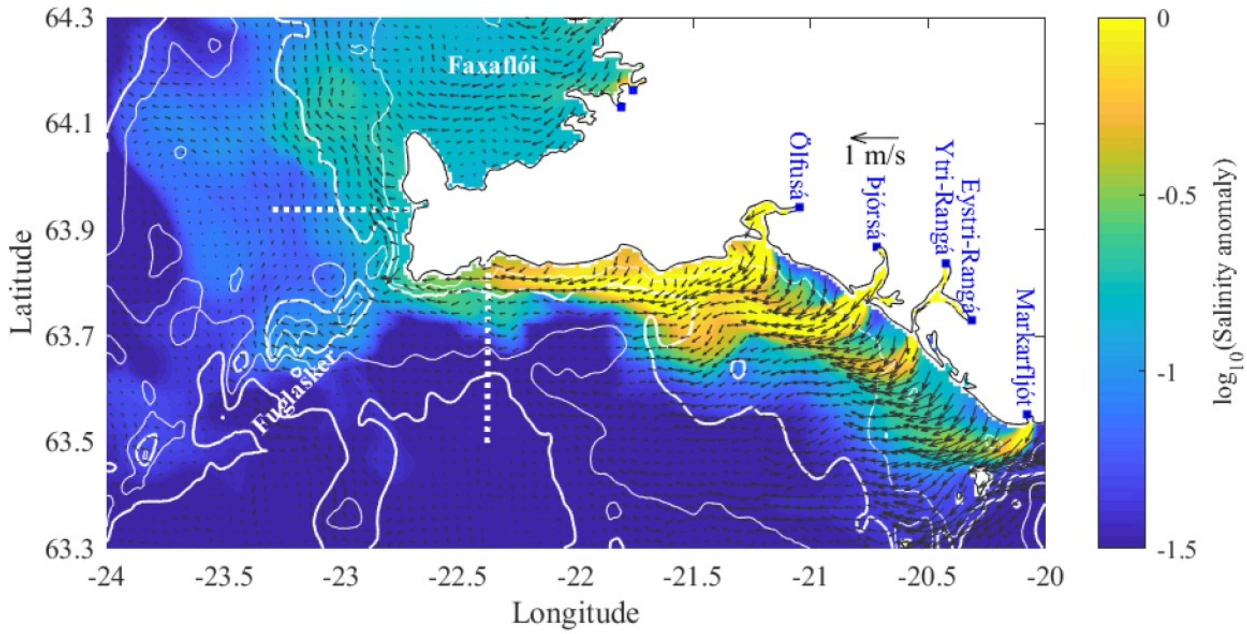

Figure 8 Surface salinity anomalies (shaded) and velocities (arrows) on 25 November 2019. Velocity vectors are subsampled to show every third data point along grid lines. The 50, 100, 150, and 200 m isobaths (white contours) and cross-section positions (white dashed) are shown. River inputs are marked (blue), rivers upshelf of the Reykjanes Peninsula are labeled (blue), and ocean place names are labeled (black).

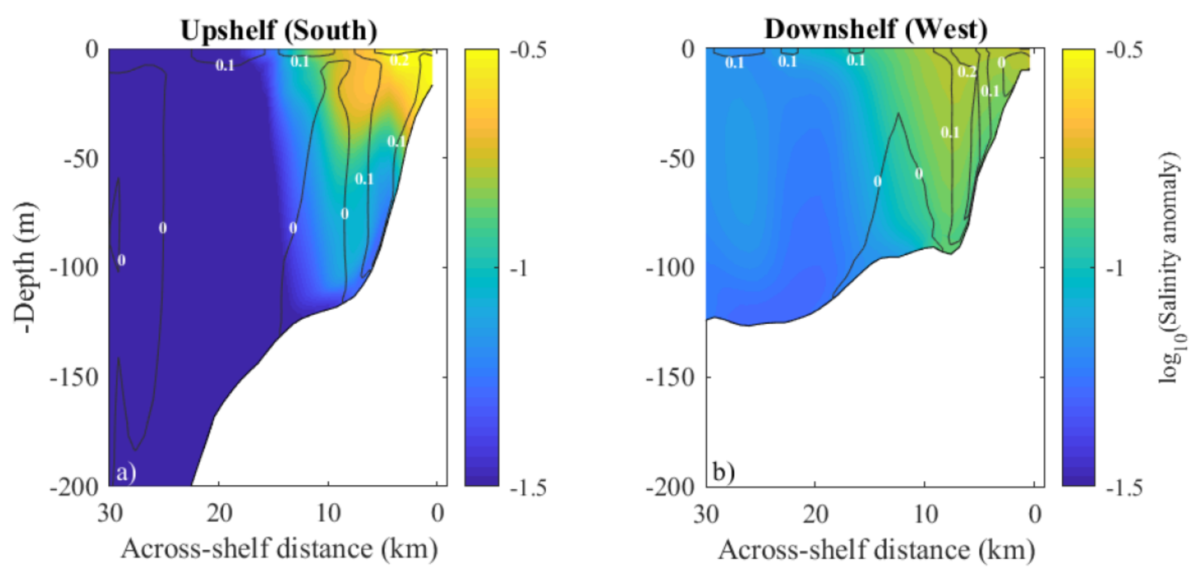

Figure 9 Salinity anomalies (shaded) and local alongshelf currents (solid and dashed lines for downshelf and upshelf flow, respectively) for 25 November 2019 at cross-shelf sections at 15 km a) upshelf or b) downshelf of Reykjanes Peninsula's southwest tip. Section locations are shown in Figure 8. Velocity contours have a 0.1 m/s interval and are labeled in white.

Under the low-wind conditions on 25 November 2019, the main ICC flow is slower and stays closer to the coast than for the strong west-southwestward wind situation on 17 October 2019. The slower flow (associated with smaller u_{wind}) reduces the r_i to 4 km, which is closer to r_c of the coast and bathymetry around the peninsula's southwest tip. Nevertheless, the inviscid theory still predicts centrifugal separation, though the corresponding overshoot would be reduced. The ICC core does separate from the coast, but bends relatively tightly around the peninsula tip with a 5 km radius of flow curvature that is only slightly larger than r_i. No eddy forms after separation, despite satisfying bulge formation conditions with $r_i>R$. The ICC still has extensive bottom contact under these conditions and bottom stress remains important. Thus, bathymetric steering guided by arrested bottom Ekman layer dynamics may influence the ICC path. The foot of the ICC (as indicated by the offshore edge of near-bottom velocities exceeding 0.1 m/s), however, shoals from near the 120 m isobath along the peninsula's south coast to shallower than the 100 m isobath offshore of the peninsula's west coast. The ICC shoals much more for weak winds than for strong west-southwestward winds. The shoaling itself and its pronounced wind dependence are inconsistent with the frictionally mediated bottom-trapping theory. The wind dependence of the ICC pathway points to the importance of wind-driven advection, which diminishes for weaker winds. The weak winds on 25 November 2019 are at most 0.03 Pa and directed approximately west-southwestward (approximately 240 °T) offshore of the peninsula's west coast. The corresponding Ekman transport is north-northwestward (approximately 330 °T). With h_e=10 m (as before), the corresponding scale for the surface Ekman velocity is at most u_{es}=0.10 m/s, which is less than 30% the magnitude on 17 October 2019 and much slower than the ICC core surface currents. The much slower wind-driven downshelf jet originating along the upshelf coast may continue beyond the peninsula tip and guide the ICC pathway; though its influence on the ICC pathway is certainly weaker than during strong winds. The 0.1-0.2 m/s southward counter flow inshore of the ICC along the peninsula's west coast is consistent with shelf circulation in response to weak upwelling-favorable winds. The wind stress component directed upshelf (southward) is 0.02 Pa (at most) and the corresponding estimate for wind-driven alongshelf flow is 0.10 m/s, which is close to the speed of the southward counter flow. The counter flow region may be narrower than during the strong west-southwestward winds because the upwelling response along the peninsula's west coast is weaker. Comparisons to sensitivity tests (described in the next section) help isolate and describe the influence winds have on the ICC pathway.

4.1.3 Other days

Six other days (06, 18, and 13 October and 13, 14, and 26 November 2019) during the study period have satellite images with enough breaks in cloud cover to detect light-colored apparently sediment-laden coastal waters (Figure 10). The band along the peninsula's south coast is approximately 10-20 km wide during all the days observed. Lighter-colored waters extend far west (30-60 km offshore) of the peninsula in all satellite images; suggesting that a wide area of coastal waters often is present offshore of the peninsula. The shape and extent of this area varies among the observed days. Modeled surface salinity anomaly and velocity fields

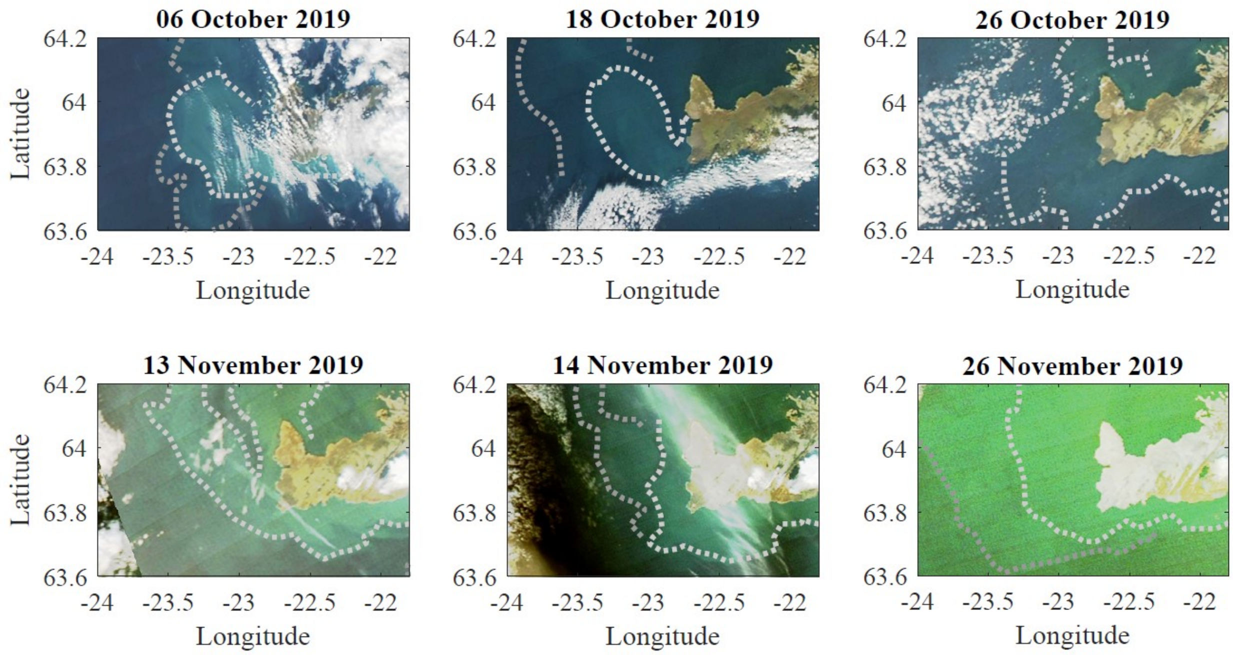

Figure 10 True-color satellite images of six additional days in the October and November 2019 study period under various river discharge and wind conditions (see Figure 4). Lighter color waters likely are associated with sediment-laden ICC waters. Approximate boundaries are sketched (dashed white and gray) based on color differences.

on these days indicate a strong dependence on wind conditions (Figure 11). The band of buoyant waters along the peninsula's south coast (with $\Delta S \geq 0.05$) is approximately 5-25 km wide. Among the highlighted days, the plume is narrowest during strong (>0.3 Pa) west-northwestward and northwestward winds with a component of the Ekman transport directed onshore. The plume is widest during strong (0.36 Pa) south-southwestward winds. The wide low salinity area (with $\Delta S \geq 0.05$) west of the peninsula extends out to 50-70 km offshore. The ΔS=0.05 outer boundary broadly corresponds to the observed light-colored coastal waters; indicating the satellite images highlight these relatively diffuse ICC waters. More concentrated ICC waters (with $\Delta S \geq 0.10$) reach at most 30 km offshore and do not appear offshore of the peninsula's west coast for three of the six days. The degree of ICC overshoot past the peninsula varies and an organized downstream eddy does not form on any of the days. Surface velocities and freshwater transport pathways are strongly wind influenced; particularly when wind stress exceeds 0.3 Pa. Sensitivity tests further describe the wind influence.

4.2 Sensitivity tests

Analysis of the sensitivity tests concentrates on comparisons for the 17 October 2019 focus time. The first sensitivity test has idealized bathymetry around the peninsula (as described in the Methods and Figure 3c) and the same forcing as the standard run with realistic bathymetry. The ranges of surface salinity anomalies in the standard run (Figure 12a) and this sensitivity run (Figure 12b) are similar. The largest ΔS values are closer to the peninsula's west coast in the

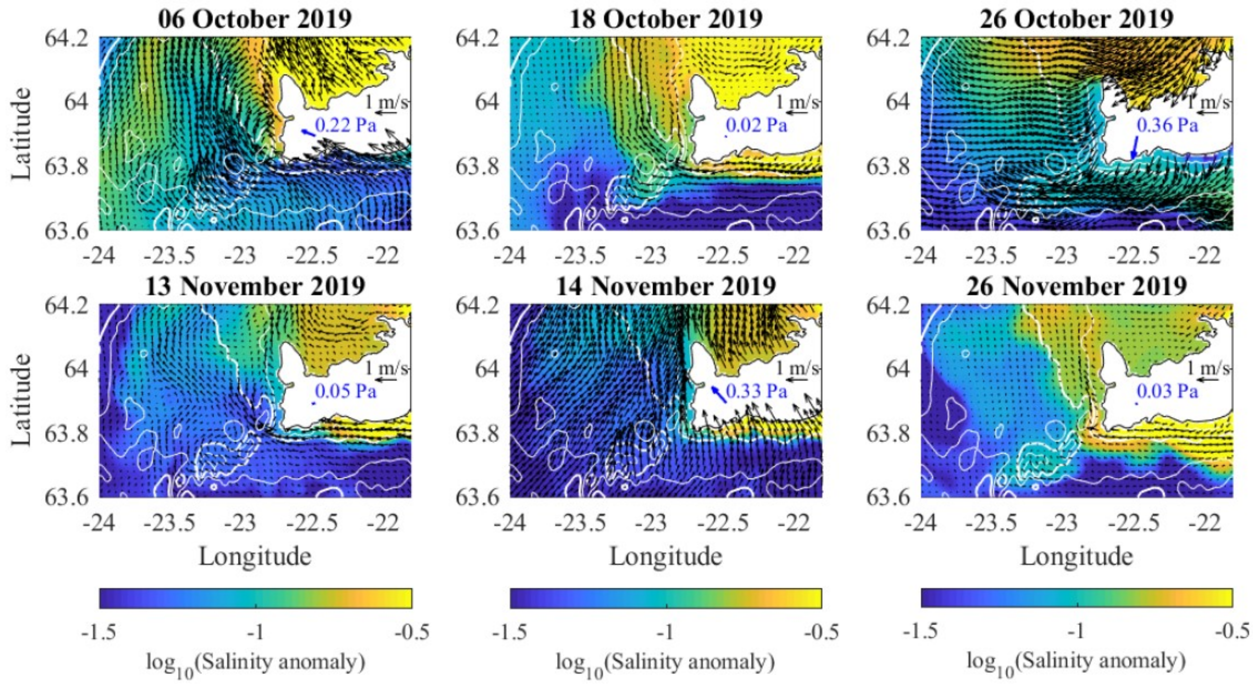

Figure 11 Surface salinity anomalies (shaded) and velocities (arrows) on the six days corresponding to satellite images in Figure 10 under a variety of forcing conditions (see Figure 4). Velocity vectors are subsampled to show every third data point along grid lines. Wind stress vectors and magnitudes (blue) in the vicinity of the peninsula are shown for each day. The 50, 100, 150, and 200 m isobaths (white contours) are shown.

idealized bathymetry run and there is no offshore deflection area with the Fuglasker removed. The ICC radius of flow curvature is much smaller (18 km) in the idealized bathymetry run than the standard run (25 km) and the center of the ICC core is approximately 6 km closer to the west coast. Both runs have counter flow with an upshelf (southward) velocity component along peninsula's west coast, but the region is more extensive in standard run. This run comparison indicates that the Fuglasker, the wide gently sloped shelf west of the peninsula, and the oblique orientation of isobaths relative to the peninsula's west coast have the combined effect of shifting the ICC offshore and causing it to bend more gradually around the peninsula. Even with the steeper idealized bathymetry with shore-parallel isobaths, the ICC separates from the coast. In the idealized bathymetry run, the ICC more quickly crosses isobaths and easily extends beyond the shelf break (200 m isobath) of the steeper and narrower shelf even though its offshore excursion is reduced.

The next sensitivity test has no wind forcing (since 02 October 2019), but other forcings and bathymetry are the same as the standard run. Salinity anomalies without winds (Figure 12c) are much larger along the ICC core (0.4-1.8) than with winds (0.1-0.3). The stronger surface buoyancy signature without wind creates stronger stratification; nevertheless, the ICC still extensively interacts with the bottom over a depth range similar to the standard run. The ICC still separates from the coast as it bends around the peninsula. The path of the ICC core has a 16

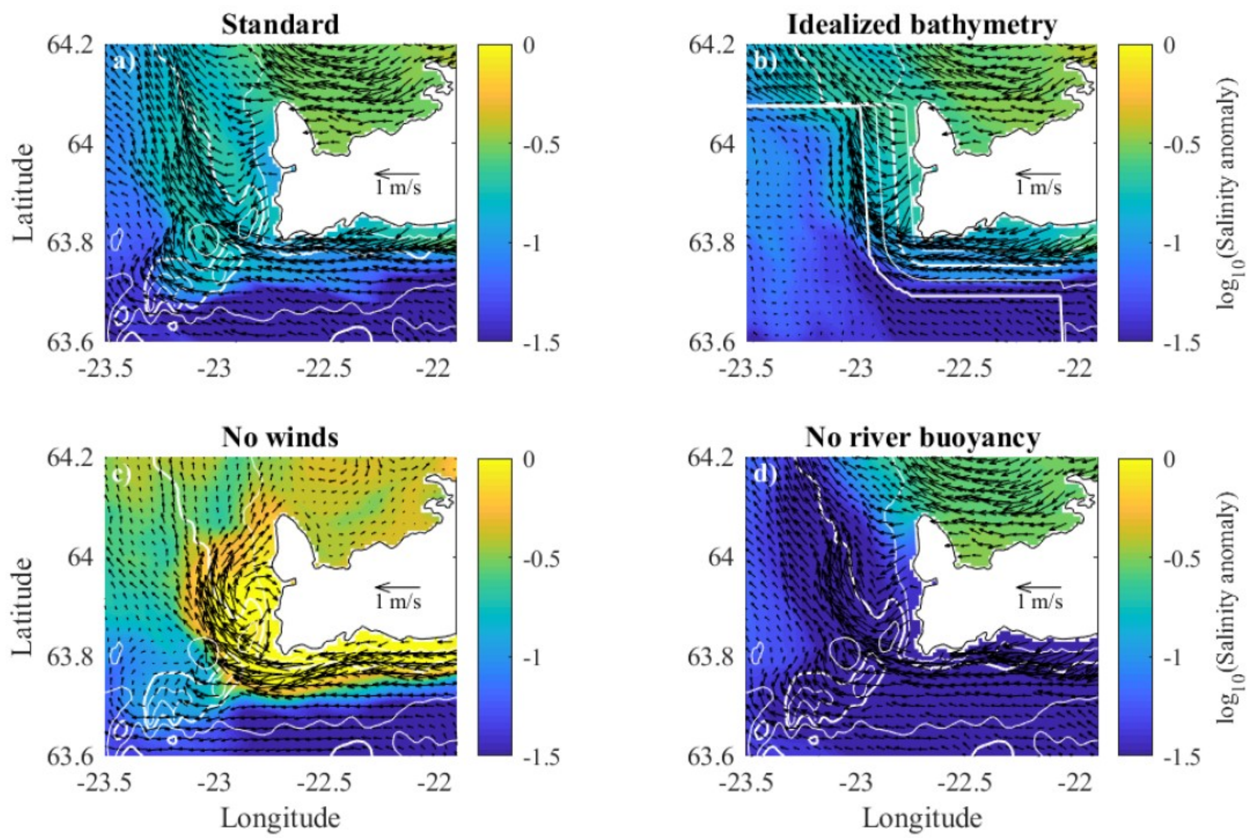

Figure 12 Surface salinity anomalies (shaded) and velocities (arrows) on 17 October 2019 for a) the standard run with realistic forcing (also shown in Figure 5) and for sensitivity tests with b) idealized constant-slope bathymetry around the peninsula, c) no winds, or d) no buoyancy inputs from rivers. Bathymetry or forcings are modified in sensitivity runs 15 days prior to the time shown. Velocity vectors are subsampled to show every third data point along grid lines. The 50, 100, 150, and 200 m isobaths (white contours) are shown.

km radius of flow curvature. Due to the tighter turn, the center of the ICC core is 5 km closer to shore than in the standard run. The ICC eventually bends back and reattaches to the coast without winds, in contrast to the path continuing offshore with winds. Both runs have counter flow with a southward component along the peninsula's west coast, but the counter flow region is constrained by the ICC's reattachment to the coast without winds. A key difference without winds is the counter flow is part of a well-formed recirculating gyre. This feature is consistent with bulge formation by buoyancy-driven plumes (Horner-Devine et al., 2006). Comparing this sensitivity test to the standard run indicates winds prevent coherent bulge formation after ICC separation from the peninsula's southwest tip.

Another sensitivity test (not shown) has idealized bathymetry around the peninsula and no wind forcing. ICC salinity anomalies in this run are as strong as in the no-wind run with realistic bathymetry. The ICC separates from the peninsula's southwest tip, but the offshore excursion of the jet is the smallest of all runs. The jet center is at least 9 km closer to the coast than the standard run. An organized recirculation area forms that is smaller and weaker than the no-wind run with the realistic bathymetry. As in the other run with idealized bathymetry, the jet quickly shifts towards deeper waters around the peninsula. Like all runs, the plume has extensive bottom contact. The three sensitivity runs collectively indicate ICC offshore excursion is enhanced both by the gently sloping and widening shelf bathymetry and by the transport driven by west-southwestward winds.

The final sensitivity test shuts off all buoyant river plumes (starting on 02 October 2019) and therefore highlights wind-driven currents. Salinity anomalies are negligible along the peninsula's south coast (Figure 12d). Thus, a buoyant ICC is absent and barotropic wind response is expected. Salinity anomalies remain large in Faxaflói and are still detectable near the peninsula's west coast. This indicates the bay is a freshwater reservoir with flushing times greater than several weeks long. Salinity anomalies also remain significant farther west of the main ICC; indicating large areas of diffuse freshwater are still present. It is this expansive region of residual coastal freshwater, rather than just the ICC core, that is evident in the light-colored apparently sediment-laden areas in the satellite images. Overall, the no-plume sensitivity run has strikingly similar surface current patterns (Figure 12d) to the standard run (Figure 12a). The chief difference is velocity magnitudes are somewhat smaller without the buoyancy-driven currents. The main wind-driven flow features include the downshelf jet along the peninsula's south coast where winds are downwelling-favorable, partial deflection around the Fuglasker, the downshelf extension of the jet that bends around the peninsula and progresses farther offshore with isobaths, a coastal band of offshore and upshelf (southward) currents along the peninsula's west coast where winds are offshore and upwelling favorable, and north-northwestward surface Ekman transport located offshore beyond the downshelf jet. It is also important to note that winds were much stronger on the previous day, therefore the wind-driven currents may be stronger than otherwise expected for the current wind conditions. The sensitivity run shows the ICC path at this time is strongly influenced by barotropic wind-driven currents that are in turn influenced by coastal and bathymetric features.

5 Discussion

Satellite ocean color images apparently showing sediment-laden riverine waters around the Reykjanes Peninsula motivate this study on ICC separation and subsequent offshore excursion from the peninsula's southwest tip and west coast. There is broad agreement between these images and the simulation results that are analyzed to further describe and diagnose ICC behavior. In some images, colors allude to concentration differences indicating where salinity anomalies likely are strongest and the ICC core flows. The simulation results are consistent with this interpretation. The satellite images generally reveal an expansive region of lightly tinged waters west of the peninsula that is many times wider than the ICC core flow. Simulation results consistently indicate large areas of relatively diffuse freshwater west of the peninsula and the ICC core. Sensitivity tests indicate this freshwater has been stripped of the main ICC flow by eddies and secondary flow pathways in the runs without winds and also mixed and transported by wind events in the runs with wind forcing. The diffuse freshwaters from the ICC are still present weeks after buoyant river plumes are shutoff in a sensitivity run; indicating the long persistence of these diffuse freshwaters, which can be detected with satellite imagery. The buildup of freshwater in nearby Faxaflói is consistent with the large freshwater thicknesses calculated from observations and simulation results (Stefánsson and Guðmundsson, 1978; Logemann et al., 2013). Model results indicate the lower salinities are associated with ICC waters and other coastal freshwaters. There is a large-scale oceanic salinity gradient between salty Atlantic water to the south and fresh Polar water to the north of Iceland that is evident in hydrographic observations, outer grid boundary conditions, and prior model results (e.g. MFRI Cruise Reports; Logemann et al., 2013; Andrews et al., 2019; Ólafsson et al., 2021). The fresh Polar water does not intrude southward on the southwest Iceland shelf; rather, the salty Atlantic water is transported northward around western Iceland by the Irminger and North Icelandic Irminger Current (e.g. Logemann et al., 2013; Ólafsson et al., 2021; Figure 2). Thus, low salinities on the southwest Iceland shelf are associated with coastal waters of riverine origin.

Several candidate mechanisms have been considered while diagnosing the ICC separation from the southwest tip of the Reykjanes Peninsula and the subsequent offshore excursion. Analysis of sensitivity tests indicates the ICC behavior without wind forcing broadly fits the inviscid theory of a baroclinic jet separating from a tightly curving coastline. Without winds, a bulge forms that recirculates some of the freshwater and increases offshore extent while most of the freshwater is transported farther downshelf in the ICC. With west-southwestward winds, the realistic and sensitivity runs indicate the ICC still separates from the peninsula's southwest tip, but there is no organized recirculating bulge. The mechanism of bathymetric steering guided by arrested bottom Ekman layer dynamics along a trapping isobath does not set the ICC pathway downstream of separation. The ICC has strong contact with the bottom and bathymetry clearly influences its path. The ICC core is much farther offshore for runs with the realistic bathymetry, which has the deflection-inducing Fuglasker (part of the Reykjanes Ridge) and a gently sloped shelf with isobaths oriented obliquely offshore of the peninsula's west coast. The bathymetric influence is exerted predominantly through shaping the wind-driven flows that guide the ICC. The barotropic wind-driven flow during west-southwestward winds includes a downshelf jet that partially deflects around the Fuglasker and bends around the peninsula while progressing farther offshore approximately with isobaths, a coastal band of offshore and upshelf flow where winds are offshore and upwelling-favorable along the peninsula's west coast, and north-northwestward surface Ekman transport located offshore beyond the downshelf jet. Analysis of satellite images and simulation results for other days during the study period illustrates ICC variability with wind conditions. Advection by the complex wind-driven flow in the vicinity of the peninsula is a main mechanism controlling the variability in velocities and offshore excursion of the ICC.

Additional research can further resolve ICC dynamics around Reykjanes Peninsula. The study area is bracketed by seasonal hydrographic observational transects (MFRI Cruise Reports), but there are no regular temperature, salinity, or current observations along the peninsula. Future studies observing salinity patterns and currents observed from moorings, ships, or autonomous platforms would pair well with the satellite observations and modeling results presented in this study. Analyzing surface drifter paths and velocities similar to Valdimarsson and Martin (1999), but with a high-resolution focus on the ICC, should provide additional information on ICC pathways and separation from the peninsula tip. Drifters recently released in the ICC region and other drifter paths in Global Drifter Program datasets (Lumpkin et al., 2019; Elipot et al., 2016; Elipot et al; 2022) can be analyzed. Drifter observations also can show tidal motion around Reykjanes Peninsula. The models in this study include M_2 tidal forcing, but the focus is not on tidal variability or tidal residual effects. Comparison of prior simulation results with and without tides hints at tidal residual flow that may favor recirculation along the peninsula's west coast (Logemann et. al., 2013), but higher-resolution analysis is required. Highlighting how the ICC is influenced by tidal mixing and currents would add to the understanding of ICC dynamics and other coastal buoyant flows.

The ICC is strongly wind-influenced during the study period. Ongoing climate change, however, has the potential to slide situations more towards buoyancy-driven effects. Iceland is a high-latitude system that is particularly sensitive to climate change and is experiencing rapid hydrological shifts. Climate change is impacting Iceland, its rivers, and the surrounding ocean. Increased glacial melting (Björnsson and Pálsson, 2008) and projected precipitation increases are changing river runoff annual cycles (Jonsdóttir, 2008; Alfieri et al., 2015) and likely increasing riverine influences in coastal waters. Nevertheless, there will continue to be many wind events strong enough to advect and mix plume waters and thereby affect ICC characteristics including its path and offshore transport around the Reykjanes Peninsula.

Iceland has many other locations where river plumes interact with abrupt changes in coastal orientation (Figure 2). After passing the Reykjanes Peninsula and Faxaflói, the ICC encounters the Snæfellsnes Peninsula and then the Westfjords region farther north, where winds likely generate equally complex wind responses and strong influences on ICC transport and mixing. Nearby to Iceland, the East Greenland Coastal Current interacts with a coastal corner at Cape Farewell (Bacon et al., 2002; Sutherland and Pickart, 2008). The coastal curvature of the cape is too gentle for inviscid coastal separation and the widening shelf plays a role in transporting some of the buoyant flow offshore to the outer shelf (Lin et al., 2018). Winds were relatively weak during the Lin et al. (2018) observational period and the average W_s was 0.2, indicating a less wind-influenced flow than the ICC conditions in the current study. Winds are often strongly downwelling-favorable (southward) along the east Greenland shelf and wind-driven export of freshwater increases at Cape Farewell (Duyck and de Jong, 2021). This export has been explained in terms of shifting wind orientation and corresponding surface Ekman transport (Duyck and de Jong, 2021), but the complete wind response likely also includes features similar to those described for Reykjanes Peninsula and the ICC.

The northwest corner of the Iberian Peninsula, with nearly perpendicular coasts meeting at Cape Finisterre, is a mid-latitude example where river plumes are influenced by winds near an abrupt coastal orientation change. One coast often experiences upwelling-favorable or downwelling-favorable conditions while the other coast does not (Alvarez et al., 2011). Multiple rivers contribute to the Western Iberian Buoyant Plume, which is strongly wind influenced (Otero et al., 2008). Plume fronts have been observed around the coastal corner during northwestward winds (Otero et al., 2009), which are downwelling-favorable along the upshelf (west) coast and offshore and upwelling-favorable along the downshelf (north) coast, similar to the ICC situation in the current study. Clouds often obscure the area from satellite observations during such wind events; this is one reason these conditions have been less studied than other situations (Otero et al., 2009). Simulations of the area (e.g. Otero et al., 2008) can support future focused analysis of plume behavior around Cape Finisterre. A low-latitude example is the Mekong River plume and the sharp coastal corner of the Mekong Delta at Ca Mau Cape. During the winter northeast monsoon season, the generally downshelf (southwestward) winds advect the buoyant coastal current along the coast towards the coastal corner (Hordoir et al., 2006). Under these winter conditions, observed and simulated drifter paths and density gradients indicate the Mekong plume likely does not tightly turn around Ca Mau Cape; it likely continues offshore beyond the cape and flows across the Gulf of Thailand mouth before obliquely entering the gulf as an important freshwater source (Stansfield and Garrett, 1997; Qian et al.,2013; Matsushita et al., 2022; Zeng et al., 2022). Simulated surface velocities indicate a widening area of low flow downshelf of the cape that is consistent with flow separation (Nguyen et al., 2022). Barotropic currents driven by similar winds only partially curve around the cape before crossing the gulf (Carmerlengo and Demmler, 1997). Thus, this Mekong plume pathway may be influenced by coastal separation at the sharp coastal corner and wind-driven currents in a fashion analogous to the situation studied for the ICC. The nearby Irrawaddy Delta also creates a coastal corner where the Irrawaddy plume continues westward offshore rather than bending around the coast during similar southwestward winds characteristic of winter monsoon conditions (Sandeep and Pant, 2019). There are other pronounced coastal orientation changes near major rivers such as the Ob, Yenisei, and Yukon that influence wind response and plume behavior (Osadchiev et al., 2017; Frey and Osadchiev, 2021; Clark and Mannino, 2022). Around the world, there are many other coastal orientation changes created by peninsulas, deltas, and other coastal corners that can lead to river plume flow separation and multi-faceted wind responses that can create hotspots of shelf-ocean exchange via offshore freshwater transport.

6 Conclusions

This study analyzes satellite observations and simulations to describe the coastal separation of the Icelandic Coastal Current from the southwest tip of the Reykjanes Peninsula. West-southwestward wind conditions are emphasized because of the observed and simulated widening and large offshore excursion of the ICC after coastal separation. Simulation results indicate there is an inner low-salinity core, mostly fed by newly introduced waters from the Ölfusá and Þjórsá rivers, within the broader ICC. The more diffuse buoyant waters stretching far offshore beyond the peninsula's west coast are older ICC waters that are not part of the new plume waters actively advancing around the peninsula. Analysis of the realistic simulation and sensitivity tests, particularly for weak- and no-wind situations, indicates the ICC separates from the peninsula's southwest tip even when purely buoyancy-driven. This behavior is consistent with inviscid theory for baroclinic flow separation from a coast that turns more tightly than the inertial radius. Bathymetric influences include the deflection of some of the ICC over the shallow Fuglasker (part of the Reykjanes Ridge) close to the peninsula's southwest tip. Comparison to sensitivity runs indicate this partial bathymetric deflection, the wide gently sloped shelf west of the peninsula, and the oblique orientation of isobaths relative to the peninsula's west coast have the combined effect of shifting the ICC offshore and causing it to bend more gradually around the peninsula. Sensitivity tests indicate the barotropic wind response to the west-southwestward winds is complicated by the abrupt change in coastal orientation and is bathymetrically influenced, but is composed of well-known elements of wind-driven dynamics. The main wind-driven flow features include the downshelf jet along the peninsula's south coast where winds are downwelling-favorable, partial deflection around the

Fuglasker, the downshelf extension of the jet that bends around the peninsula and progresses farther offshore with isobaths, a band of offshore and upshelf (southward) currents along the peninsula's west coast where winds are offshore and upwelling-favorable, and north-northwestward surface Ekman transport located offshore beyond the downshelf jet. Advection by the complex wind-driven flow in the vicinity of the peninsula is a main mechanism controlling the velocities and offshore excursion of the ICC during the study period. The ICC during weak winds is slower, turns more tightly around the peninsula's southwest tip, still separates from the coast, partially deflects around the Fuglasker, and flows much closer along the peninsula's west coast. Thus, ICC offshore excursion is markedly increased by winds blowing obliquely offshore from the southwest tip of the Reykjanes Peninsula. Similar wind-influenced scenarios likely occur for other river plumes interacting with peninsulas, deltas, and other coastal corners. Such situations most likely are hotspots for offshore freshwater transport and shelf-ocean exchange.

Acknowledgements

This research was supported by an Iceland Fulbright – NSF Arctic Research Scholar grant, a University of Connecticut Research Excellence Program grant, and NSF Ocean Sciences Physical Oceanography grant 1756578. The manuscript was revised with the helpful comments and suggestions of the editor and two anonymous reviewers. The Iceland Fulbright Commission, Snæbjörn Pálsson, and Páll Ríkharðsson helped during the Fulbright experience in Iceland.

References

Alfieri, L., Burek, P., Feyen, L. and Forzieri, G., 2015. Global warming increases the frequency of river floods in Europe. *Hydrol. Earth Syst. Sci.*, 19(5), 2247-2260. https://doi.org/10.5194/hess-19-2247-2015

Alvarez, I., Gomez-Gesteira, M., DeCastro, M., Lorenzo, M. N., Crespo, A. J. C. and Dias, J. M., 2011. Comparative analysis of upwelling influence between the western and northern coast of the Iberian Peninsula. *Cont. Shelf Res.*, 31(5), 388-399. https://doi.org/10.1016/j.csr.2010.07.009

Amante, C. and B. W. Eakins, 2009. *ETOPO1 1 Arc-Minute Global Relief Model: Procedures, Data Sources and Analysis*. NOAA Technical Memorandum NESDIS NGDC-24. National Geophysical Data Center, NOAA. https://doi.org/10.7289/V5C8276M

Andrews, J. T., Jónsdóttir, I., and Geirsdóttir, Á., 2019. Tracking Holocene drift-ice limits on the northwest–southwest Iceland shelf: Comparing proxy data with observation and historical evidence. *Arctic, Antarctic, and Alpine Research*, 51, 96-114, https://doi.org/10.1080/15230430.2019.1592648

Bacon, S., Reverdin, G., Rigor, I. G. and Snaith, H. M., 2002. A freshwater jet on the east Greenland shelf. *J. Geophys. Res.: Oceans*, 107(C7), 5-1. https://doi.org/10.1029/2001JC000935

Ball, F. K., 1965. Second-class motions of a shallow liquid. *J. Fluid Mech.*, 23(3), 545-561. https://doi.org/10.1017/S0022112065001532

Björnsson, H. and Pálsson, F., 2008. Icelandic glaciers. *Jökull*, 58, 365-386. http://jardvis.hi.is/sites/jardvis.hi.is/files/Pdf_skjol/Jokull58_pdf/jokull58-bjornssonpalsson.pdf

Bormans, M., and C. Garrett, 1989: A simple criterion for gyre formation by the surface outflow from a strait, with application to the Alboran Sea. *J. Geophys. Res.*, 94, 12 637–12 644. https://doi.org/10.1029/JC094iC09p12637

Brink, K. H., 2016. Cross-shelf exchange. *Ann. Rev. Mar. Sci.*, 8, 59-78. https://doi.org/10.1146/annurev-marine-010814-015717

Burger, A. P., 1958. Scale Consideration of Planetary Motions of the Atmosphere. *Tellus*, 10(2), 195-205. https://doi.org/10.3402/tellusa.v10i2.9236

Camerlengo, A., and Demmler, M. I., 1997. Wind-driven circulation of peninsular Malaysia's eastern continental shelf. *Scientia Marina*, 61, 203-211. http://scimar.icm.csic.es/scimar/index.php/secId/6/IdArt/2851/

Cenedese, C. and J. A. Whitehead, 2000. Eddy Shedding from a Boundary Current around a Cape over a Sloping Bottom. *J. Phys. Oceanogr.*, 30(7), 1514-1531. https://doi.org/10.1175/1520-0485(2000)030<1514:ESFABC>2.0.CO;2

Chant, R. J., 2011. Interactions between estuaries and coasts: river plumes—their formation transport and dispersal. In *Treatise on Estuarine and Coastal Science*, Vol. 2, ed. E. Wolanski, D. McLusky, pp. 213–35. Amsterdam: Elsevier. https://doi.org/10.1016/B978-0-12-374711-2.00209-6

Chapman, D. C., 1985. Numerical treatment of cross-shelf open boundaries in a barotropic coastal ocean model. *J. Phys. Oceanogr.*, 15(8), 1060-1075. https://doi.org/10.1175/1520-0485(1985)015<1060:NTOCSO>2.0.CO;2

Chapman, D. C., 2003. Separation of an advectively trapped buoyancy current at a bathymetric bend. *J. Phys. Oceanogr.*, 33(5), 1108-1121. https://doi.org/10.1175/1520-0485(2003)033<1108:SOAATB>2.0.CO;2

Chassignet, E. P., Hurlburt, H. E., Smedstad, O. M., Halliwell, G. R., Hogan, P. J., Wallcraft, A. J., Baraille, R., and Bleck, R., 2007. The HYCOM (hybrid coordinate ocean model) data assimilative system. *J. Mar. Syst.*, 65(1-4), 60-83. https://doi.org/10.1016/j.jmarsys.2005.09.016

Chen, Z., Jiang, Y., Wang, J. and Gong, W., 2019. Influence of a River Plume on Coastal Upwelling Dynamics: Importance of Stratification. *J. Phys. Oceanogr.*, 49(9), 2345-2363. https://doi.org/10.1175/JPO-D-18-0215.1

Clark, J. B. and Mannino, A., 2022. The Impacts of Freshwater Input and Surface Wind Velocity on the Strength and Extent of a Large High Latitude River Plume. *Frontiers in Mar. Sci.*, 8, https://doi.org/10.3389/fmars.2021.793217

Davis, R. E. and Bogden, P. S., 1989. Variability on the California shelf forced by local and remote winds during the Coastal Ocean Dynamics Experiment. *J. Geophys. Res.: Oceans*, 94(C4), 4763-4783. https://doi.org/10.1029/JC094iC04p04763

Dittmar, T., and Kattner, G., 2003. The biogeochemistry of the river and shelf ecosystem of the Arctic Ocean: a review. *Mar. Chem.*, 83(3-4), 103-120. https://doi.org/10.1016/S0304-4203(03)00105-1

Duyck, E. and De Jong, M. F., 2021. Circulation over the South-East Greenland Shelf and potential for liquid freshwater export: a drifter study. *Geophys. Res. Lett.*, 48(5), e2020JB020886. https://doi.org/10.1029/2020GL091948

Egbert, G. D., and Erofeeva, S. Y., 2002. Efficient inverse modeling of barotropic ocean tides. *J. Atmosph. Oceanic Tech.*, 19(2), 183-204. https://doi.org/10.1175/1520-0426(2002)019<0183:EIMOBO>2.0.CO;2

Elipot, S., Sykulski, A., Lumpkin, R., Centurioni, L., and Pazos, M., 2022. *Hourly location, current velocity, and temperature collected from Global Drifter Program drifters world-wide*. NOAA National Centers for Environmental Information. Dataset. https://doi.org/10.25921/x46c-3620.

Elipot, S., Lumpkin, R., Perez, R. C., Lilly, J. M., Early, J. J., and Sykulski, A. M., 2016, A global surface drifter dataset at hourly resolution, *J. Geophys. Res.: Oceans*, 121, https://doi:10.1002/2016JC011716.

Fanning, D. W., 2009. Bright MODIS Images, *Coyote's Guide to IDL Programming: Discovering the Possibilities*, http://www.idlcoyote.com/ip_tips/brightmodis.html

Flather, R. A., 1976. A tidal model of the northwest European continental shelf. *Memoires de la Societe Royale des Sciences de Liege*, 10(6), 141–164.

Fong, D. A. and Geyer, W. R., 2001. Response of a river plume during an upwelling favorable wind event. *J. Geophys. Res.: Oceans*, 106(C1), 1067-1084. https://doi.org/10.1029/2000JC900134

Frey, D. and Osadchiev, A., 2021. Large River Plumes Detection by Satellite Altimetry: Case Study of the Ob–Yenisei Plume. *Remote Sens.*, 13(24), 5014. https://doi.org/10.3390/rs13245014

Garrett, C., 1995. Flow separation in the ocean. In *Topographic Effects in the Ocean: Proceedings of the 8th 'Aha Huliko'a Hawaiian Winter Workshop*, P. Müller and D. Henderson (eds.), School of Ocean and Earth Science and Technology, University of Hawaii, 119-124. https://apps.dtic.mil/sti/pdfs/ADA327289.pdf

Garvine, R. W., 1995. A dynamical system for classifying buoyant coastal discharges, *Cont. Shelf Res.*, 15(13), 1585–1596. https://doi.org/10.1016/0278-4343(94)00065-U

Griffin, D. A. and Middleton, J. H., 1991. Local and remote wind forcing of New South Wales inner shelf currents and sea level. *J. Physical Oceanogr.*, 21(2), 304-322. https://doi.org/10.1175/1520-0485(1991)021<0304:LARWFO>2.0.CO;2

Grimes, C. B., 2001. Fishery production and the Mississippi River discharge. *Fisheries*, 26(8), 17-26. https://doi.org/10.1577/1548-8446(2001)026<0017:FPATMR>2.0.CO;2

Haidvogel, D. B., Arango, H., Budgell, W. P., Cornuelle, B. D., Curchitser, E., Di Lorenzo, E., Fennel, K., Geyer, W. R., Hermann, A. J., Lanerolle, L., Levin, J., McWilliams, J. C., Miller, A. J., Moore, A. M., Powell, T. M., Shchepetkin, A. F., Sherwood, C. R., Signell, R. P., Warner, J. C., and Wilkin, J., 2008. Ocean forecasting in terrain-following coordinates: Formulation and skill assessment of the Regional Ocean Modeling System. *J. Computational Physics*, 227(7), 3595-3624. https://doi.org/10.1016/j.jcp.2007.06.016

Haidvogel, D. B., Arango, H. G., Hedstrom, K., Beckmann, A., Malanotte-Rizzoli, P., and Shchepetkin, A. F., 2000. Model evaluation experiments in the North Atlantic Basin: Simulations in nonlinear terrain-following coordinates. *Dynam. Atmos. Oceans*, 32, 239–281. https://doi.org/10.1016/S0377-0265(00)00049-X

Hetland R. D., and Hsu T. -J., 2013. Freshwater and sediment dispersal in large river plumes. In *Biogeochemical Dynamics at Large River-Coastal Interfaces: Linkages with Global Climate Change*, ed.

T. S. Bianchi, M. A. Allison, W. –J. Cai, pp. 55–85. New York: Springer. https://doi.org/10.1017/CBO9781139136853

Hickey, B. M., Kudela, R. M., Nash, J. D., Bruland, K. W., Peterson, W. T., MacCready, P., Lessard, E. J., Jay, D. A., Banas, N. S., Baptista, A. M., and Dever, E. P., 2010. River influences on shelf ecosystems: introduction and synthesis. *J. Geophys. Res.: Oceans*, 115(C2). https://doi.org/10.1029/2009JC005452

Hordoir, R., Nguyen, K. D. and Polcher, J., 2006. Simulating tropical river plumes, a set of parametrizations based on macroscale data: A test case in the Mekong Delta region. *J. Geophys. Res.: Oceans*, 111, C09036 . https://doi.org/10.1029/2005JC003392

Horner-Devine, A. R., Fong, D. A., Monismith, S. G. and Maxworthy, T., 2006. Laboratory experiments simulating a coastal river inflow. *J. Fluid Mech.*, 555, 203-232. https://doi.org/10.1017/S0022112006008937

Horner-Devine, A. R., Hetland, R. D., and MacDonald, D. G., 2015. Mixing and transport in coastal river plumes. *Ann. Rev. Fluid Mech.*, 47, 569-594. https://doi.org/10.1146/annurev-fluid-010313-141408

Hunter, E. J., Chant, R. J., Wilkin, J. L., and Kohut, J., 2010. High-frequency forcing and subtidal response of the Hudson River plume. *J. Geophys. Res.: Oceans*, 115, C07012, https://doi.org/10.1029/2009JC005620

Icelandic Meteorological Office, 2021. *Hydrology data*. Accessed February 2021. https://en.vedur.is/#tab=hydro

Jiang, X., 1995. *Flow separation by interfacial upwelling in the coastal ocean*. M.S. thesis, School of Earth and Ocean Sciences, University of Victoria, 55 pp.

Jonsdottir, J. F., 2008. A runoff map based on numerically simulated precipitation and a projection of future runoff in Iceland/Une carte d'écoulement basée sur la précipitation numériquement simulée et un scénario du futur écoulement en Islande. *Hydrol. Sci. J.*, 53(1), 100-111. https://doi.org/10.1623/hysj.53.1.100

Jurisa, J. T., and Chant, R. J., 2013. Impact of offshore winds on a buoyant river plume system. *J. Phys. Oceanogr.*, 43(12), 2571-2587. https://doi.org/10.1175/JPO-D-12-0118.1

Klinger, B. A., 1994. Inviscid current separation from rounded capes. *J. Phys. Oceanogr.*, 24, 1805–1811. https://doi.org/10.1175/1520-0485(1994)024<1805:ICSFRC>2.0.CO;2

Lentz, S., 2004. The response of buoyant coastal plumes to upwelling-favorable winds. *J. Phys. Oceanogr.*, 34(11), 2458-2469. https://doi.org/10.1175/JPO2647.1

Lentz, S. J. and Helfrich, K. R., 2002. Buoyant gravity currents along a sloping bottom in a rotating fluid. *J. Fluid Mech.*, 464(1), 251-278. https://doi.org/10.1017/S0022112002008868

Lentz, S. J. and J. Largier, 2006. The Influence of Wind Forcing on the Chesapeake Bay Buoyant Coastal Current. *J. Phys. Oceanogr.*, 36(7), 1305-1316. https://doi.org/10.1175/JPO2909.1

Lin, P., Pickart, R. S., Torres, D. J. and Pacini, A., 2018. Evolution of the freshwater coastal current at the southern tip of Greenland. *J. Phys. Oceanogr.*, 48(9), 2127-2140. https://doi.org/10.1175/JPO-D-18-0035.1

Lin, P., Pickart, R. S., Jochumsen, K., Moore, G. W. K., Valdimarsson, H., Fristedt, T. and Pratt, L. J., 2020. Kinematic Structure and Dynamics of the Denmark Strait Overflow from Ship-Based Observations. *J. Phys. Oceanogr.*, 50(11), 3235-3251. https://doi.org/10.1175/JPO-D-20-0095.1

Logemann, K., Ólafsson, J., Snorrason, Á., Valdimarsson, H. and Marteinsdóttir, G., 2013. The circulation of Icelandic waters-a modelling study. *Ocean Sci. Discuss.*, 10(2). https://doi.org/10.5194/os-9-931-2013

Loughlin, C., Mendes, A. R. M., Morrison, L. and Morley, A., 2021. The role of oceanographic processes and sedimentological settings on the deposition of microplastics in marine sediment: Icelandic waters. *Mar. Poll. Bull.*, 164, 111976. https://doi.org/10.1016/j.marpolbul.2021.111976

Lumpkin, R. and Centurioni, L., 2019. *Global Drifter Program quality-controlled 6-hour interpolated data from ocean surface drifting buoys*. NOAA National Centers for Environmental Information. Dataset. https://doi.org/10.25921/7ntx-z961.

MacCready, P. and Rhines, P. B., 1993. Slippery bottom boundary layers on a slope. *J. Phys. Oceanogr.*, 23(1), 5-22. https://doi.org/10.1175/1520-0485(1993)023<0005:SBBLOA>2.0.CO;2

Malmberg, S. A. and Kristmannsson, S. S., 1992. Hydrographic conditions in Icelandic waters, 1980 1989. *ICES Mar. Sci. Symp.*, 195, 76–92. http://www.ices.dk/sites/pub/Publication%20Reports/Marine%20Science%20Symposia/ICES%20Marine%20Science%20Symposia%20-%20Volume%20195%20-%201992%20-%20Part%2009%20of%2050.pdf

Marine & Freshwater Research Institute (MFRI), *Cruise Reports, Salinity sections for Selvogsbanki and Faxaflói transects, 1997-2020*. https://sjora.hafro.is/

Matsushita, K., Y. Uchiyama, N. Takaura, and T. Kosako, 2022. Fate of river-derived microplastics from the South China Sea: Sources to surrounding seas, shores, and abysses. *Env. Poll.*, 308, 119631. https://doi.org/10.1016/j.envpol.2022.119631

McWilliams, J. C., E. Huckle, and A. Shchepetkin, 2009. Buoyancy Effects in a Stratified Ekman Layer, *J. Phys. Oceanogr.*, 39(10), 2581-2599. https://doi.org/10.1175/2009JPO4130.1

Mendes, R., Vaz, N., Fernández-Nóvoa, D., Da Silva, J. C. B., Decastro, M., Gómez-Gesteira, M. and Dias, J. M., 2014. Observation of a turbid plume using MODIS imagery: The case of Douro estuary (Portugal). *Remote Sens. Environ.*, 154, 127-138. https://doi.org/10.1016/j.rse.2014.08.003

Meybeck, M., 2003. Global analysis of river systems: from Earth system controls to Anthropocene syndromes. *Philos. Trans. Royal Soc. Lond. B: Biol. Sci.*, 358(1440), 1935-1955. https://doi.org/10.1098/rstb.2003.1379

Milliman, J. D. and Farnsworth, K. L., 2013. *River Discharge to the Coastal Ocean: A Global Synthesis.* Cambridge University Press. https://doi.org/10.1017/CBO9780511781247

Moffat, C. and S. Lentz, 2012. On the Response of a Buoyant Plume to Downwelling-Favorable Wind Stress. *J. Phys. Oceanogr.*, 42(7), 1083-1098. https://doi.org/10.1175/JPO-D-11-015.1

Mysak, L. A., 1980. Recent Advances in Shelf Wave Dynamics. *Rev. Geophys. Space Phys.*, 18(1), 211-241. https://doi.org/10.1029/RG018i001p00211

Nguyen, N. M., San, D. C., Nguyen, K. D., Pham, Q. B., Gagnon, A. S., Mai, S. T. and Anh, D. T., 2022. Region of freshwater influence (ROFI) and its impact on sediment transport in the lower

Mekong Delta coastal zone of Vietnam. *Environ. Monit. Assess.*, 194(7), 1-15. https://doi.org/10.1007/s10661-022-10113-9

O'Donnell, J., 2010. The dynamics of estuary plumes and fronts. In *Contemporary Issues in Estuarine Physics*, ed. A Valle Levinson, pp. 186–246. Cambridge, UK: Cambridge Univ. Press. https://doi.org/10.1017/CBO9780511676567

Ólafsson, J., Ólafsdóttir, S. R., and Briem, J., 2008. Vatnsföll og vistkerfi strandsjávar, *Náttúrufræðingurinn*, 76, 95–108. https://www.researchgate.net/publication/303074343_Vatnsfoll_og_vistkerfi_strandsjavar

Ólafsson, J., Ólafsdóttir, S. R., Takahashi, T., Danielsen, M. and Arnarson, T. S., 2021. Enhancement of the North Atlantic CO 2 sink by Arctic Waters. *Biogeosciences*, 18(5), 1689-1701. https://doi.org/10.5194/bg-18-1689-2021

Orlanski, I., 1976. A simple boundary condition for unbounded hyperbolic flows. *J. Comput. Phys.*, 21(3), 251-269. https://doi.org/10.1016/0021-9991(76)90023-1

Osadchiev, A. A., Izhitskiy, A. S., Zavialov, P. O., Kremenetskiy, V. V., Polukhin, A. A., Pelevin, V. V. and Toktamysova, Z. M., 2017. Structure of the buoyant plume formed by Ob and Yenisei river discharge in the southern part of the Kara Sea during summer and autumn. *J. Geophys. Res.: Oceans*, 122(7), 5916-5935. https://doi.org/10.1002/2016JC012603

Osadchiev, A. A., and Zavialov, P. O., 2013. Lagrangian model of a surface-advected river plume. *Cont. Shelf Res.*, 58, 96-106. https://doi.org/10.1016/j.csr.2013.03.010

Otero, P., Ruiz-Villarreal, M. and Peliz, A., 2008. Variability of river plumes off Northwest Iberia in response to wind events. *J. Mar. Syst.*, 72(1-4), 238-255. https://doi.org/10.1016/j.jmarsys.2007.05.016

Otero, P., Ruiz-Villarreal, M. and Peliz, A., 2009. River plume fronts off NW Iberia from satellite observations and model data. *ICES J. Mar. Sci.*, 66(9), 1853-1864. https://doi.org/10.1093/icesjms/fsp156

Ou, H. W., 1980. On the propagation of free topographic Rossby waves near continental margins. Part 1: Analytical model for a wedge. *J. Phys. Oceanogr.*, 10(7), 1051-1060. https://doi.org/10.1175/1520-0485(1980)010<1051:OTPOFT>2.0.CO;2

Phillips, N. A., 1963. Geophysical Motion. *Rev. Geophys.*, 1(2), 123-176. https://doi.org/10.1029/RG001i002p00123

Pringle, J. M., 2002. Enhancement of wind-driven upwelling and downwelling by alongshore bathymetric variability. *J. Phys. Oceanogr.*, 32(11), 3101-3112. https://doi.org/10.1175/1520-0485(2002)032<3101:EOWDUA>2.0.CO;2

Qian, Y. K., Peng, S. and Li, Y., 2013. Eulerian and Lagrangian statistics in the South China Sea as deduced from surface drifters. *J. Phys. Oceanogr.*, 43(4), 726-743. https://doi.org/10.1175/JPO-D-12-0170.1

Reyes-Mendoza, O., Marino-Tapia, I., Herrera-Silveira, J., Ruiz-Martínez, G., Enriquez, C. and Largier, J. L., 2016. The effects of wind on upwelling off Cabo Catoche. *J. Coastal Res.*, 32(3), 638-650. https://doi.org/10.2112/JCOASTRES-D-15-00043.1

Sandeep, K. K. and Pant, V., 2019. Riverine freshwater plume variability in the Bay of Bengal using wind sensitivity experiments. *Deep Sea Res. Part II: Topical Studies in Oceanogr.*, 168, 104649. https://doi.org/10.1016/j.dsr2.2019.104649

Stansfield, K. and Garrett, C., 1997. Implications of the salt and heat budgets of the Gulf of Thailand. *J. Mar. Res.*, 55(5), 935-963. https://doi.org/10.1357/0022240973224184

Stefánsson, U., and Guðmundsson, G., 1978. The Freshwater Regime of Faxaflói, Southwest Iceland, and its Relationship to Meteorological Variables. *Estuar. Coast. Mar. Sci.*, 6, 535-551. https://doi.org/10.1016/0302-3524(78)90030-0

Stefánsson, U., and Ólafsson, J., 1991. Nutrients and fertility of Icelandic waters. *Rit Fiskideildar*, 12: 1–56. https://www.landsvirkjun.com/Media/rit_fisk_123.pdf

Stock, C. A., John, J. G., Rykaczewski, R. R., Asch, R. G., Cheung, W. W., Dunne, J. P., Friedland, K. D., Lam, V. W., Sarmiento, J. L. and Watson, R. A., 2017. Reconciling fisheries catch and ocean productivity. *Proceed. Nat. Acad. Sci.*, 114(8), E1441-E1449. https://doi.org/10.1073/pnas.1610238114

Sutherland, D. A. and Pickart, R. S., 2008. The East Greenland coastal current: Structure, variability, and forcing. *Prog. Oceanogr.*, 78(1), 58-77. https://doi.org/10.1016/j.pocean.2007.09.006

Valdimarsson, H. and Martin, S.-A., 1999. Near-surface circulation in Icelandic waters derived from satellite tracked drifters. *Rit Fiskideildar*, 16, 23-29. https://www.hafogvatn.is/static/research/files/rit_fisk_1999_xvi_03.pdf

Vilhjálmsson, H., 2002. Capelin (*Mallotus villosus*) in the Iceland–East Greenland–Jan Mayen ecosystem. – *ICES J. Mar. Sci.*, 59: 870–883. https://doi.org/10.1006/jmsc.2002.1233

Whitney, M. M., 2022. *Supporting Data for Separation of the Icelandic Coastal Current from the Reykjanes Peninsula*, Mendeley Data, V1, https://doi.org/10.17632/w6fvv9jtpw.1.

Whitney, M. M. and Garvine, R. W., 2005. Wind influence on a coastal buoyant outflow. *J. Geophys. Res.: Oceans*, 110(C3). https://doi.org/10.1029/2003JC002261

Wu, H., and Zhu, J., 2010. Advection scheme with 3rd high-order spatial interpolation at the middle temporal level and its application to saltwater intrusion in the Changjiang Estuary. *Ocean Modell.*, 33, 33–51. https://doi.org/10.1016/j.ocemod.2009.12.001

Yang, J., and Chen, K. 2021. The role of wind stress in driving the alongshelf flow in the northwest Atlantic Ocean. *J. Geophys. Res.: Oceans*, 126, e2020JC016757. https://doi.org/10.1029/2020JC016757

Yankovsky, A. E. and Chapman, D. C., 1997. A simple theory for the fate of buoyant coastal discharges. *J. Phys. Oceanogr.*, 27(7), 1386-1401. https://doi.org/10.1175/1520-0485(1997)027<1386:ASTFTF>2.0.CO;2

Zeng, X., Bracco, A. and Tagklis, F., 2022. Dynamical impact of the Mekong River plume in the South China Sea. *J. Geophys. Res.: Oceans*, 127(5), e2021JC017572. https://doi.org/10.1029/2021JC017572